On the modelling of heat and fluid transport in fibrous porous media: Analytical fractal models for permeability and thermal conductivity

Tian Xiao [a], Junfei Guo [b], Xiaohu Yang [b,*], Kamel Hooman [c], Tian Jian Lu [d,e,**]

[a] State Key Laboratory for Strength and Vibration of Mechanical Structures, School of Aerospace, Xi'an Jiaotong University, Xi'an, 710049, PR China
[b] Institute of the Building Environment & Sustainability Technology, School of Human Settlements and Civil Engineering, Xi'an Jiaotong University, Xi'an, 710049, PR China
[c] School of Mechanical and Mining Engineering, The University of Queensland, Brisbane, QLD, 4072, Australia
[d] State Key Laboratory of Mechanics and Control of Mechanical Structures, Nanjing University of Aeronautics and Astronautics, Nanjing, 210016, PR China
[e] MIIT Key Laboratory of Multifunctional Lightweight Materials and Structures (MLMS), Nanjing University of Aeronautics and Astronautics, Nanjing, 210016, PR China

ARTICLE INFO

ABSTRACT

Building upon fractal theory and relying exclusively on analytical models, we develop models for predicting the permeability and effective thermal conductivity of two-directional (2-D) fibrous porous materials. In contrast to previous permeability and conductivity models, two hypothetical parameters (β and ζ) with physical meaning are introduced to consider the contact thermal resistance at the fiber interfaces, and analytical models for both in-plane and out-of-plane directions are developed. Relevant geometrical and physical parameters, including porosity, average tortuosity, and thermal resistance, are obtained by modeling the representative structure (RS) of the fibrous porous material. Good agreement with existing experimental data for fibrous materials over a wide range of porosity (from 0.50 to 0.99) validates the developed models, for both the permeability and effective thermal conductivity. It is demonstrated that, compared with previous models based on simplified geometries relying on periodic distribution assumptions, the current fractal model can better characterize the randomness of pore size and distribution commonly found in commercial fibrous materials.

1. Introduction

High porosity fibrous materials typically exhibit low density, formability, high specific area, and high thermal conductivity, among other attributes [1–4], thus widely applied in the fields of electronics devices [5], thermal energy storage [6], heat transfer enhancement materials [7], insulation [8], chemical catalyst [9], fuel cells [10], aerospace transportation system [11], porous burner [12], waste heat recovery [13] and biomedical applications [14]. In such applications, the permeability and effective thermal conductivity of fibrous porous materials are key parameters affecting heat and fluid flow through the material. To characterize fibrous porous materials, numerous analytical, numerical and experimental studies have been carried out. Nonetheless, given the complex geometric morphology found in most commercial fibrous materials, using analytical methods to accurately determine their permeability and effective thermal conductivities remains a challenge. To meet the challenge, using fractal theory, we develop analytical models of predicting the permeability and effective thermal conductivity of two-directional (2-D) fibrous porous materials. To this end, as shown schematically in Fig. 1, we assume that the axes of the 2D fibrous structure are located in planes parallel to each other, and the positions and orientations of the cylindrical, infinitely long fibers are randomly distributed in these planes. Therefore, the 2-D fibrous materials considered are transversely isotropic such that models for both - in plane and out-of-plane directions need to be developed.

Since the fibrous material of Fig. 1(b) is composed of randomly distributed fibers that form interconnected pores, directly solving the Navier-Stokes equations to obtain its permeability, or the Laplace heat conduction equation to obtain its effective thermal conductivity, is almost impossible. It is thus necessary to develop approximate theoretical schemes, not only for designing the morphology of the fibrous material for specific applications, but also for exploring physical mechanisms underlying its thermofludic characteristics. In previous

---

* Corresponding author.
** Corresponding author. State Key Laboratory of Mechanics and Control of Mechanical Structures, Nanjing University of Aeronautics and Astronautics, Nanjing, 210016, PR China.
E-mail addresses: xiaohuyang@xjtu.edu.cn (X. Yang), tjlu@nuaa.edu.cn (T.J. Lu).

Nomenclature

Symbols

a	Weight value
d	Microscopic length scale(m)
d_E	Euclidean dimension
d_s	Ligament thickness(m)
d_p	Pore diameterofrepresentative structure(m)
D_f	Fractal dimension of the pore size distribution
D_T	Fractal dimension of average tortuosity
K	Permeability (m^2)
l	Length (m)
L_0	Characteristic length (m)
P	Perimeter of cross − section (m)
p	Pressure (Pa)
S	Cross sectional area (m^2)

V	Volume (m^3)
V_{total}	Total volume (m^3)
V_{pore}	Pore volume (m^3)

Greek symbols

μ	Dynamic viscosity (Pa·s)
λ	Pore diameter (m)
ε	Porosity
τ	Tortuosity

Subscript

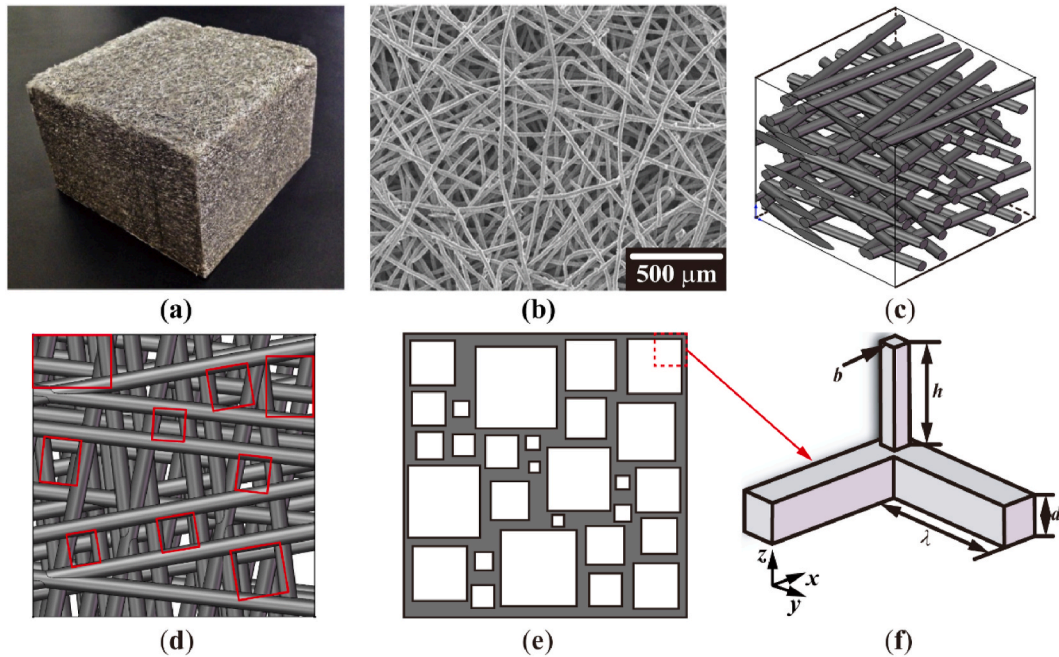|	
av	Average
max	Maximum
min	Minimum
RS	Representative structure
t	Total

Fig. 1. Structure of 2-D fibrous material: (a) photo of fiber felt [11]; (b) scanning electronic microscope (SEM) image [23]; (c) isometric view of fibrous material with random in-plane fiber orientation; (d) top view of fibrous material with random in-plane fiber orientation; (e) schematic of fibrous porous material with square pore and randomly-distributed solid ligaments; (f) representative structure (RS) for 2-D fibrous material.

studies, for simplification, the complicated porous structure is usually assumed to be periodically distributed and a unit cell (UC) or part of the UC is selected to represent both the topological and morphological features of a bulk porous material. Two typical methods have been employed to determine the permeability and conductivity of a fibrous porous material. On the one hand, upon assuming that the randomly-distributed pore structure is represented by packed spheres, the permeability and thermal conductivity can be obtained by modifying the Kozeny-Carmen equation [15–17] and extending the Maxwell-Eucken equation [18], respectively. Empirical constants are nonetheless present in the Kozeny-Carmen model for permeability and in the Maxwell-Eucken model for conductivity [15–17,19,20], which vary from one porous material to another. On the other hand, to account for the effect of fibrous microstructure, periodically distributed square, staggered and hexagonal arrays, and cubic lattice trusses have been adopted to construct the UC. The method of volume-averaging is then used to solve the Hagen-Poiseuille flow to obtain the permeability [21, 22], while the thermal resistance network model is employed to model heat conduction in the UC [23]. There exists a multitude of predictive models for the permeability [16,17,20–22] and effective thermal conductivity [23] of fibrous materials. Often, however, these models are made possible through the use of simplifying assumptions, thus incapable of accounting for the randomness in the size and distribution of pores. For typical instance, the 2-D fibrous porous material of Fig. 1 is directional, with its permeability and effective thermal conductivity differing in the in-plane and out-of-plane directions. However, previous theoretical studies assumed that the permeability and conductivity do not vary with direction [24,25], which contradicted available experimental data [26,27]. Therefore, for a 2-D fibrous porous material, new analytical models that can better reflect the stochastic nature of its pore size and distribution, as well as accurately predict its permeability and effective thermal conductivity in both in-plane and out-of-plane

directions, are needed, as attempted in the current study.

One approach is to use fractal theory. It has been confirmed that fractal theory can describe and characterize the transport properties of porous media containing randomly distributed pores, such as fibrous materials [28], particulate porous media [29], cellular metal foams [30], Sierpinski structures [31,32], soil [33], oil/gas reservoir [34], etc. Therefore, considering that the pore structure, size, and distribution in a fibrous material are typically random, and that the pores have similar properties within a certain scale range, issues such as disorderly arranged pores, tortuous flow, and heat conduction at pore scale may be addressed using the fractal theory, as it enables accurate prediction of permeability [28,34–37] and effective thermal conductivity [14,29,32, 38] of porous media.

An analytical expression for the permeability of bi-dispersed porous media was established by applying the fractal distribution of capillaries to a capillary bundle model [35], being a generalized expression for the permeability [39] of porous media based on fractal theory. Subsequent theoretical studies have continuously enriched existing knowledge of physical mechanisms underlying transport flow in fractal porous media. Consequently, the effects of key parameters such as fractal porosity and pore volume distribution [40], tortuosity [35,41], maximum pore size [42], size distribution of contact areas [43], saturation of unsaturated porous media [44,45], and surface roughness [46] on fluid transport and permeability for various types of porous medium have been quantified and expressed analytically, as summarized in recent reviews [36,47]. In addition to the before-mentioned progress in fractal theory for fluid transport in porous media, numerical simulations based on, e.g., automata lattice gas (LG) [48], finite element (FM) method [49], effective medium theory [50], numerical reconstruction of real porous media [51], Lattice Boltzmann Method (LBM) [52], Monte Carlo simulation [53], have also been applied to simulate and calculate the permeability of porous media.

Thus far, the effective thermal conductivity of a porous medium has been obtained by experimental measurements and numerical simulations of heat transfer through its complex microstructure. However, such experimental measurements and numerical simulations are often approximate and do not provide a deep understanding of heat conduction mechanisms in porous media. Therefore, finding analytical expressions for the effective thermal conductivity of porous media becomes an attractive and challenging research direction. Volkov and Zhigilei [54–56] developed the theoretical analysis and numerical calculations of the effective thermal conductivity of random fiber materials. Although the fibers they studied are mainly for nanofiber materials, they also provide a new way to study the effective thermal conductivity of random fiber materials. In recent years, it has been demonstrated that the fractal theory provides a new method to predict the effective thermal conductivity of porous media having random pore sizes and distributions, such as particulate porous media [29], porous rocks [57], soil [58], tree-like bifurcated structures [59], and fibrous materials [60]. In particular, the geometric percolation model has been incorporated into the fractal theory to analyze thermal transport in porous media [61,62]. Another alternative is make use of the fractal characteristics of a porous media (e.g., microstructure, pore size, and distribution of pores), so that its effective thermal medium can be expressed as a function of porosity and parameters representing microstructures [29,32]. As to fibrous materials, although attempts of using fractal theory to predict the effective thermal conductivity have started, relevant parameters still need to be tuned based on the specific fibrous structure considered. Further research is therefore needed to improve the prediction accuracy of fractal theory and the applicability of thermal conductivity model for 2-D fibrous materials.

In summary, previous investigations indicated that fractal theory plays an important role in understanding fluid and heat transport phenomena in porous media, enabling in-depth study of permeability and effective thermal conductivity. However, little attention has been paid to the fractal characteristics of fibrous materials and the validity of using

fractal theory to develop permeability and conductivity models against experimental measurements. In the current study, to address this deficiency, focusing upon 2-D fibrous materials (Fig. 1), we apply pore-scale geometric characterizations to construct analytical fractal models for permeability and effective thermal conductivity, and validate the model predictions against existing test data.

2. Theoretical model

2.1. Theory for fractal porous media

The fractal theory is developed to describe pore size that is distributed in a fractal fashion in a porous medium [63,64]. With reference to Fig. 1, given the microstructural features of a 2-D fibrous material, the fractal theory dictates that [63]:

$$M(l) \propto l^{D_f} \tag{1}$$

where $M(l)$ denotes the measure of a fractal porous medium, l is the representative scale, and D_f represents its fractal dimension. It follows that the number N and size λ of pores in the porous medium satisfy the fractal law, given by Ref. [35]:

$$N(l \geq \lambda) = (\lambda_{\max}/\lambda)^{D_f} \tag{2}$$

where $\lambda_{\max}$ represents the maximum pore size in the porous medium and $N(l \geq \lambda)$ is the number of pores whose pore sizes are greater than or equal to λ. If the pore size λ is replaced by the minimum pore size $\lambda_{\min}$, then the total number of pores N_t can be expressed as [35]:

$$N_t(l \geq \lambda_{\min}) = (\lambda_{\max}/\lambda_{\min})^{D_f} \tag{3}$$

Therefore, the numebr of pores in the infinitesimal range of λ to $\lambda + d\lambda$ can be obtained by differentiating Eq. (2) [28,64], as:

$$-dN = D_f \lambda_{\max}^{D_f} \lambda^{-(D_f+1)} d\lambda \tag{4}$$

where $-dN > 0$. That is, the number of pores decreases with increasing pore size. Relative to the total pore count, the percentage of the number of pores in the range from λ to $\lambda + d\lambda$ can be obtained by dividing (4) by (3), resulting in:

$$-\frac{dN}{N_t} = D_f \lambda_{\min}^{D_f} \lambda^{-(D_f+1)} d\lambda = f(\lambda) d\lambda \tag{5}$$

where $f(\lambda) = D_f \lambda_{\min}^{D_f} \lambda^{-(D_f+1)}$ is the probability density function of pores in the porous medium [35,40]. According to the probability theory, the law obtained by integrating the probability density function satisfies the normalization [35,40]:

$$\int_{-\infty}^{+\infty} f(\lambda) d\lambda = \int_{\lambda_{\min}}^{\lambda_{\max}} f(\lambda) d\lambda = 1 - \left(\frac{\lambda_{\min}}{\lambda_{\max}}\right)^{D_f} \equiv 1 \tag{6}$$

The prerequisite for Eq. (6) is

$$\left(\frac{\lambda_{\min}}{\lambda_{\max}}\right)^{D_f} \cong 0 \tag{7}$$

Equations (1)–(7) lay the theoretical foundation for fractal porous media, with Eq. (7) serving as the fundamental premise for applying the fractal geometry theory [40].

2.2. Fractal model of permeability

Based on the fractal theory, a generalized expression for fractal permeability can be obtained by assuming that the flow rate of fluid through tortuous circular capillary tubes in a porous medium satisfies the modified Hagen-Poiseulle equation, as [35]:
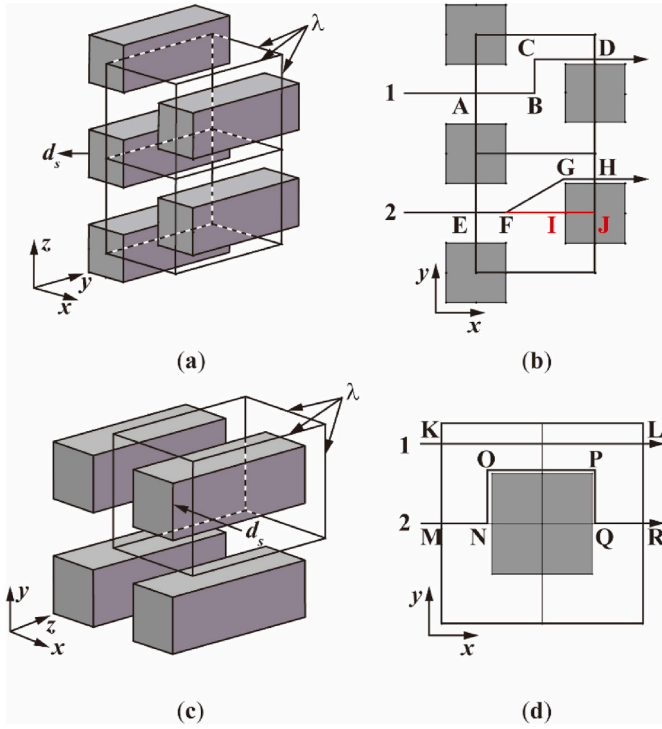
Fig. 2. Distribution of streamlines as seen from different angles of view: (a) three-dimensional configuration for square ligaments in a dislocated and equidistant arrangement and the corresponding unit cell; (b) side view of streamlines flowing around square ligaments in a dislocated and equidistant arrangement; (c) three-dimensional configuration for square ligaments in a square arrangement and the corresponding unit cell; (d) side view of streamlines flowing around square ligaments in a square arrangement.

$$K = \frac{\pi}{128} \frac{L_0^{1-D_T}}{A} \frac{D_f}{3 + D_T - D_f} \lambda_{\max}^{3+D_T} \tag{8}$$

where A is the unit cross-sectional area of a fractal pore set, L_0 is the characteristic length containing all the fractal pores (from the smallest to the largest diameter), $\lambda_{\max}$ is the maximum pore diameter, D_T denotes the fractal dimension of average tortuosity, and D_f represents the fractal dimension of pore size distribution. An expression of D_f was further proposed, as [40]:

$$D_f = d_E - \frac{\ln \varepsilon}{\ln(\lambda_{\min}/\lambda_{\max})} \tag{9}$$

where ε is the porosity, and d_E is the Euclidean dimension, e.g., $d_E = 2, 3$ are the two- and three-dimensional space, in respective. Therefore, for two-dimensional space, $1 < D_f < 2$; for three-dimensional space, $2 < D_f < 3$.

For a 2-D fibrous material, using the model of Eq. (8) to predict its permeability requires the determination of three key parameters: L_0, D_T and $\lambda_{\max}$.

2.2.1. Characteristic length L_0

Within the characteristic length L_0, all the fractal pores (from the smallest to the largest) are included. For a cubic fibrous material with side length L_0, the porosity can be expressed as:

$$\varepsilon = \frac{V_{pore}}{L_0^3} \tag{10}$$

where V_{pore} is the total volume of pores in the porous medium. In the current study, for simplicity, the pores are modeled as ideal spherical pores such that the total pore volume can be calculated as [36,65]:

$$V_{pore} = \frac{\pi D_{f,3} \lambda_{\max}^3}{6(3 - D_{f,3})} (1 - \varepsilon) \tag{11}$$

where $D_{f,3} = 3 - \frac{\ln \varepsilon}{\ln(\lambda_{\min}/\lambda_{\max})}$. The characteristic length L_0 can thence be obtained as:

$$L_0 = \lambda_{\max} \left[\frac{\pi D_{f,3}}{6(3 - D_{f,3})} \frac{1 - \varepsilon}{\varepsilon} \right]^{\frac{1}{3}} \tag{12}$$

2.2.2. Unit cross-sectional area A

Fig. 1(a) and (b) depict both sample photographs and scanning electron microscopic (SEM) images for a typical fiber felt. Not only the solid ligaments but also the complex pores are seen to be randomly distributed (Fig. 1(b)) in the fibrous material, following the fundamental assumption of fractal theory. Axes of the 2-D random fibers are located in planes parallel to each other, with positions and orientations randomly distributed in these planes, as shown in Fig. 1(c) and (d). The anisotropic fibrous material is formed by stacking each layer of such randomly distributed fibers, thus exhibiting two main directions: in-plane and out-of-plane. To simplify the current analytical modeling, idealized square pores in each layer of the fibrous material are assumed, with random sizes and distributions, as shown in Fig. 1(e). Among the disordered pores, the joint with three struts (Fig. 1(f)) is selected as the representative structure (RS) for subsequent characterization analysis, and the circular fiber is simplified into the square. Let λ, b, d_s and h represent separately the pore size, width, ligament thickness, and height of the RS. In Fig. 1(f), a different ligament in the z-direction of the representative structure is introduced to consider the thermal contact resistance between different fiber layers. The thermal contact resistance between 2-D fiber layers is estimated quantitatively by two hypothesis parameters b and h (i.e., $\beta = b/d_s$ and $\zeta = h/\lambda$).

(a) In-plane

The total (in-plane) cross-sectional area is given by Ref. [66]:

$$A_{in} = \frac{A_{p\_in}}{\varepsilon} = \frac{\pi D_{f,2} \lambda_{\max}^2 (1 - \varepsilon)}{4(2 - D_{f,2}) \varepsilon} \tag{13}$$

where $D_{f,2} = 2 - \frac{\ln \varepsilon}{\ln(\lambda_{\min}/\lambda_{\max})}$.

(b) Out-of-plane

The pores in Fig. 1(e) may be considered as squares with varying size (λ), such that the total pore area A_{p_out} in the out-of-plane direction may be calculated as:

$$A_{p\_out} = -\int_{\lambda_{\min}}^{\lambda_{\max}} a\lambda dN = \frac{D_{f,2} \lambda_{\max}^2}{(2 - D_{f,2})} (1 - \varepsilon) \tag{14}$$

Then, the total (out-of-plane) cross-sectional area A_{out} is:

$$A_{out} = \frac{A_{p\_out}}{\varepsilon} = \frac{D_{f,2} \lambda_{\max}^2 (1 - \varepsilon)}{(2 - D_{f,2}) \varepsilon} \tag{15}$$

2.2.3. Fractal dimension of average tortuosity D_T

The macroscopic transport parameters of a porous medium are commonly related to its tortuosity, i.e., the tortuous path of fluid flow. To represent the tortuosity of fluid flow through the present 2-D fibrous material of Fig. 1, we approximate the tortuous paths as a bundle of tortuous capillary tubes. Thus, using the analytical method for determining the fractal dimension (D_T) of average tortuosity detailed in Ref. [67], we obtain:

$$D_T = 1 + \frac{\ln \tau_{av}}{\ln(L_0/\lambda_{av})} \tag{16}$$

where λ_{av} and τ_{av} are the average pore diameter and avergae tortuosity, respectively. Here, $D_T = 1$ represents a straight channel/tube, $D_T = 2$ represents a tortuous channel/tube that fills the two-dimensional space, and $D_T = 3$ represents a tortuous channel/tube that fills the three-dimensional space. Therefore, $1 < D_T < 2$ for a two-dimensional porous medium, and $1 < D_T < 3$ for a three-dimensional porous medium.

The average pore diameter of a porous medium can be calculated using the fractal theory combined with the probability density function, as [67]:

$$\lambda_{av} = \frac{D_{f,3}\lambda_{\min}}{D_{f,3} - 1} \tag{17}$$

When $D_{f,3}$ and L_0 are determined, the only key parameter that needs to be solved is the average tortuosity τ_{av}. The tortuosity of a porous medium is defined as the ratio of the actual length for the real tortuous flow path to the straight (minimal) length [68,69]. However, calculating the tortuosity of each tortuous path to get the average tortuosity is prohibitively difficult. It had nonetheless been proven that the average tortuosity could be estimated using the average of representative streamlines [70]. For a 2-D fibrous material, Fig. 2 depicts the distribution of two representative streamlines in its RS. Two representative structures of ligaments distribution are selected, as shown in Fig. 2(a) and (c)). In reality, the distribution of ligaments is complicated because the fibrous material is composed of randomly distributed fibers. Accordingly, to further simplify the calculation, both misaligned ligaments and equidistant ones are used to calculate the tortuosity as well as to simplify the irregularly distributed ligaments into a square arrangement, as depicted in Fig. 2(a) and (c).

The average tortuosity is obtained by a weighted average of all possible streamlines around two representative structure ligaments, as demonstrated in Fig. 2(b) and (d), yielding:

$$\tau_{av} = \sum_{i=1}^{n} a_i \tau_i \tag{18}$$

where a is the weight value ($\sum_{i=1}^{n} a_i = 1$), τ_i is the tortuosity of the i-th flow streamline, and n is the total number of possible streamlines. When $a_1 = a_2 = \cdots = a_n$, Eq. (18) is reduced to a simple statistical average [70]. Generally speaking, given that a good deal of flow paths exist in an RS, finding and calculating all the fluid flow pathlines to obtain average tortuosity is almost impossible. Alternatively, it has been suggested [70] that the average tortuosity is related to the weighted averaged tortuosity for two representative flow paths: the longest and the shortest. For the representative structure (RS) of 2-D fibrous material, the numerical values of its length, width, height of are equal to λ, and the thickness of ligaments is d_s, as shown in Fig. 2(a) and (c). Therefore, the pore volume of the RS can be calculated as:

$$V_{RS-pore} = \lambda^3 - \lambda \cdot d_s^2 \tag{19}$$

while its total volume is:

$$V_{RS-total} = \lambda^3 \tag{20}$$

It follows that its porosity is given by:

$$\varepsilon = \frac{V_{RS-pore}}{V_{RS-total}} = 1 - \left(\frac{d_s}{\lambda}\right)^2 \tag{21}$$

from which

$$\frac{\lambda_s}{\lambda} = \sqrt{1 - \varepsilon} \tag{22}$$

For streamline 1 in Fig. 2(b), $l_{AB} = l_{CD} = \frac{\lambda}{2}$ and $l_{BC} = \frac{d_s}{2}$. According to

the definition of tortuosity, the tortuosity of streamline 1 can be expressed as:

$$\tau_{1-1} = \frac{l_{AB} + l_{BC} + l_{CD}}{l_{AB} + l_{CD}} = 1 + \frac{1}{2}\frac{\lambda_s}{\lambda} = 1 + \frac{\sqrt{1 - \varepsilon}}{2} \tag{23}$$

Similarly, for streamline 2 in Fig. 2(b), as $l_{EF} = l_{GH} = l_{IJ} = l_{GI} = d_s/2$, $l_{FI} = \lambda - d_s$ and $l_{FG} = \sqrt{l_{GI}^2 + l_{FI}^2} = \sqrt{\left(\frac{d_s}{2}\right)^2 + (\lambda - d_s)^2}$, its tortuosity can be obtained as:

$$\tau_{1-2} = \frac{l_{EF} + l_{FG} + l_{GH}}{l_{EF} + l_{FI} + l_{IJ}} = \frac{d_s + \sqrt{\left(\frac{d_s}{2}\right)^2 + (\lambda - d_s)^2}}{d} = \sqrt{1-\varepsilon} + \frac{1}{2}\sqrt{9 - 5\varepsilon - 8\sqrt{1-\varepsilon}} \tag{24}$$

For the distribution of solid ligaments depicted in Fig. 2(b), the weights of streamlines 1 and 2 are not affected by changes in porosity. No matter how the porosity is varied, streamlines 1 and 2 have the same weight: $a_{1-1} = a_{1-2}$ and $a_{1-1} + a_{1-2} = 1$. Therefore, the tortuosity can be obtained by using a simple weighted average, as:

$$\tau_1 = a_{1-1}\tau_{1-1} + a_{1-2}\tau_{1-2} = \frac{1}{2}\tau_{1-1} + \frac{1}{2}\tau_{1-2}$$
$$= \frac{2 + 3\sqrt{1-\varepsilon} + \sqrt{9 - 5\varepsilon - 8\sqrt{1-\varepsilon}}}{4} \tag{25}$$

where a_{1-1} and a_{1-2} are the value of the weight of streamlines 1 and 2, respectively.

For streamline 1 in Fig. 2(d), the actual length l_{GH} and the straight length of flow l_{GH} are equal, yielding:

$$\tau_{2-1} = \frac{l_{GH}}{l_{GH}} = 1 \tag{26}$$

With reference to Fig. 2(d), since boundary thickness is thin on ligament surface, streamline 2 of the ligament boundary layer is thought to fit the ligament surface, as $l_{MN} = l_{QR} = \frac{\lambda}{2}$, $l_{NO} = l_{PQ} = \frac{d_s}{2}$ and $l_{OP} = d_s$. The tortuosity of streamline 2 can thus be calculated by:

$$\tau_{2-2} = \frac{l_{MN} + l_{NO} + l_{OP} + l_{PQ} + l_{QR}}{l_{MN} + l_{OP} + l_{QR}} = \frac{\lambda + d_s}{\lambda} = 1 + \sqrt{1-\varepsilon} \tag{27}$$

In Fig. 2(d), the streamline is tortuous near the ligament but almost straight further away from it. As the porosity decreases, the ligament number density (per volume) increases, leading to less straight streamlines and more tortuous ones. The two weights for streamlines 1 and 2 in Fig. 2(d) are $a_{2-1} = \frac{\lambda^3 - \lambda d_s^2}{\lambda^3}$ and $a_{2-2} = \frac{\lambda d_s^2}{\lambda^3}$, respectively. Therefore, the average tortuosity τ_2 in Fig. 2(d) can be derived as:

$$\tau_2 = a_{2-1}\tau_{2-1} + a_{2-2}\tau_{2-2} = \left(\frac{\lambda^3 - \lambda d_s^2}{\lambda^3}\right)\tau_{2-1} + \frac{\lambda d_s^2}{\lambda^3}\tau_{2-2} = 1 + (1-\varepsilon)\sqrt{1-\varepsilon} \tag{28}$$

In the present 2-D fibrous material, the pores are randomly distributed with varying pore sizes. Consequently, in practice, the proportions of the two ligament distributions shown in Fig. 2(a) and (c) cannot be directly measured. We therefore assume that the two distributions have the same proportion, i.e., $a_1 = a_2 = \frac{1}{2}$, a_1 being the weight value for the dislocated and equidistant arrangement of Fig. 2(a) and a_2 the weight value for the square arrangement of Fig. 2(c). According to Eqs. (25) and (28), the average tortuosity is finalized as:

$$\tau_{av} = a_1\tau_1 + a_2\tau_2 = \frac{1}{2}\tau_1 + \frac{1}{2}\tau_2 = \frac{6 + (7 - 4\varepsilon)\sqrt{1-\varepsilon} + \sqrt{9 - 5\varepsilon - 8\sqrt{1-\varepsilon}}}{8} \tag{29}$$

Eventually, from Eqs. (12), (16), (17) and (29), the fractal dimension of average tortuosity is obtained as:
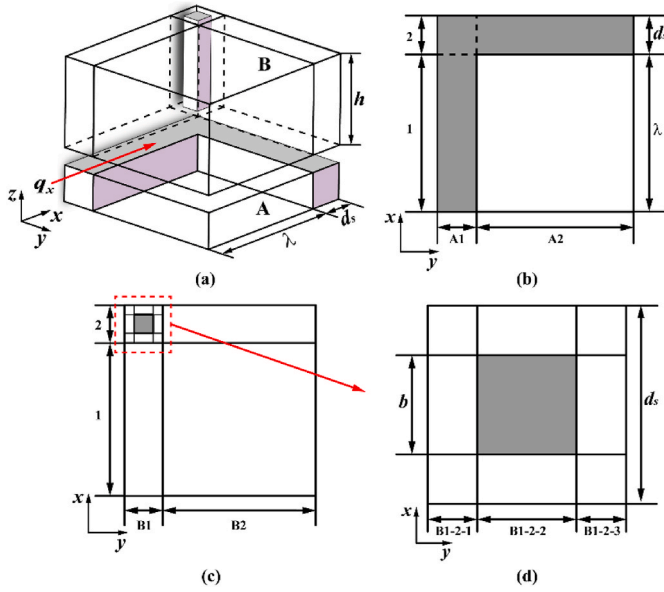
Fig. 3. Idealized pore structure model of 2-D fibrous material: (a) schematic of in-plane heat conduction; (b) top view of layer A in RS; (c) top view of layer B in RS; (d) top view of layer B1-2 in RS.
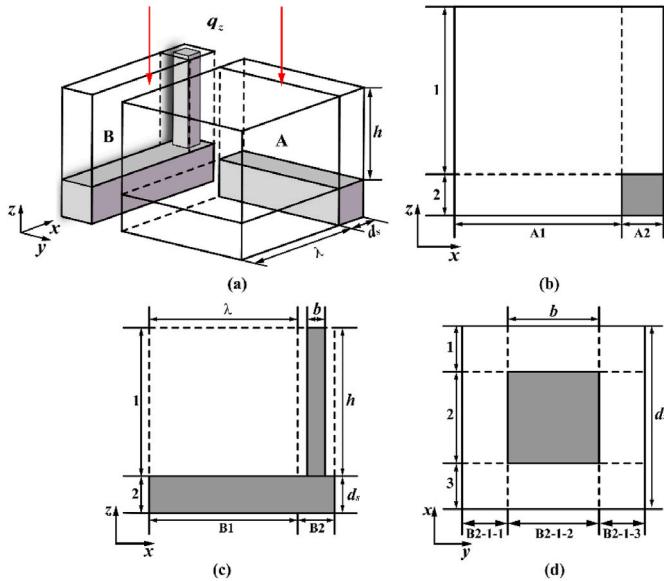

Fig. 4. Idealized pore structure model of fibrous material: (a) schematic of out-of-plane heat conduction; (b) front view of layer A in RS; (c) front view of layer B in RS; (d) top view of layer B1-2 in RS.

$$D_T = 1 + \frac{\ln\left\{\frac{1}{8}\left[6 + (7-4\varepsilon)\sqrt{1-\varepsilon} + \sqrt{9 - 5\varepsilon - 8\sqrt{1-\varepsilon}}\right]\right\}}{\ln\left\{\frac{\lambda_{\max}}{\lambda_{\min}} \frac{D_{f,3}-1}{D_{f,3}}\left[\frac{\pi D_{f,3}}{6(3-D_{f,3})}\frac{1-\varepsilon}{\varepsilon}\right]^{\frac{1}{3}}\right\}} \tag{30}$$

2.2.4. The maximum pore diameter

(a) In-plane

With fractal theory, the pores of different sizes in a porous medium have similar shapes. Therefore, the largest pore volume corresponds to the maximum pore size. In the in-plane direction of the present fibrous material, with the cross-sectional shape of the stacked fibers taken as

circular, it is assumed that the pore shape in the in-plane direction is mainly cylindrical. An equivalent cylindrical pore is therefore used to approximate the pore shape in the in-plane direction. It follows that the maximum pore volume $V_{\max-p}$ can be expressed as:

$$V_{\max-p} = \pi\left(\frac{h_{\max}}{2}\right)^2\lambda_{\max} = \frac{\pi}{4}\zeta^2\lambda_{\max}^3 = V_{tp} - V_s = V_s\frac{\varepsilon}{1-\varepsilon} \tag{31}$$

where $V_{tp} = \frac{V_s}{1-\varepsilon}$ is the total volume, and V_s is the volume of solid ligaments (i.e., fibers) given by:

$$V_s = (2\lambda + d_s)d_s^2 + hb^2 \tag{32}$$

According to Eqs. (31) and (32), the maximum equivalent pore diameter in the in-plane direction is:

$$\lambda_{\max} = d_s\left[\frac{4(2+\gamma+\zeta\beta^2)\varepsilon}{\pi\zeta^2\gamma(1-\varepsilon)}\right]^{\frac{1}{3}} \tag{33}$$

where $d_s = \gamma\lambda$, $b = \beta d_s$ and $h = \zeta\lambda$.

(b) Out-of-plane

For the out-of-plane direction, the shape of the pores (which is determined mainly by randomly distributed fibers) is assumed to be rectangular, as shown in Fig. 1(e). The maximum pore volume $V_{\max-p}$ is thence:

$$V_{\max-p} = h_{\max}\lambda_{\max}^2 = \zeta\lambda_{\max}^3 = V_{tp} - V_s = V_s\frac{\varepsilon}{1-\varepsilon} \tag{34}$$

where $V_{tp} = \frac{V_s}{1-\varepsilon}$ and V_s are the total volume of pores and the volume of solid ligaments, respectively. According to Eqs. (32) and (34), the maximum equivalent pore diameter $\lambda_{\max}$ in the out-of-plane direction is given by:

$$\lambda_{\max} = d_s\left[\frac{(2+\gamma+\zeta\beta^2)\varepsilon}{\alpha\zeta\gamma(1-\varepsilon)}\right]^{\frac{1}{3}} \tag{35}$$

2.2.5. The porosity

For 2-D fibrous materials, the porosity ε can be calculated as:

$$\varepsilon = 1 - \frac{V_s}{V_t} = 1 - \frac{\gamma^2(2+\gamma+\zeta\beta^2)}{(1+\gamma)^2(\zeta+\gamma)} \tag{36}$$

where $\gamma = d_s/\lambda$ $(0 < \gamma \le 1)$, $\beta = b/d_s(0 < \beta \le 1)$ and $\zeta = h/\lambda$ $(0 < \zeta \le 1)$.

2.2.6. Permeability correlation

(a) In-plane

Upon determining all key parameters as detailed above, the in-plane permeability of 2-D fibrous materials can be determined as:

$$\frac{K}{d_s^2} = \frac{1}{32}\frac{(2-D_{f,2})}{(3+D_T-D_{f,2})}\frac{\varepsilon}{(1-\varepsilon)}\left[\frac{\pi D_{f,3}}{6(3-D_{f,3})}\frac{(1-\varepsilon)}{\varepsilon}\right]^{\frac{1-D_T}{3}}\left[\frac{4(2+\gamma+\zeta\beta^2)\varepsilon}{\pi\zeta^2\gamma(1-\varepsilon)}\right]^{\frac{2}{3}} \tag{37}$$

(b) Out-of-planeSimilarly, the out-of-plane permeability can be correlated as:

$$\frac{K}{d_s^2} = \frac{\pi}{128}\frac{(2-D_{f,2})}{(3+D_T-D_{f,2})}\frac{\varepsilon}{(1-\varepsilon)}\left[\frac{\pi D_{f,3}}{6(3-D_{f,3})}\frac{(1-\varepsilon)}{\varepsilon}\right]^{\frac{1-D_T}{3}}\left[\frac{(2+\gamma+\zeta\beta^2)\varepsilon}{\zeta\gamma(1-\varepsilon)}\right]^{\frac{2}{3}} \tag{38}$$

where $D_{f,2} = 2 - \frac{\ln\varepsilon}{\ln(\lambda_{\min}/\lambda_{\max})}$ and $D_{f,3} = 3 - \frac{\ln\varepsilon}{\ln(\lambda_{\min}/\lambda_{\max})}$.

It should be pointed out that, the above analytical model, obtained

based on the fractal theory and a set of simplifying assumptions concerning the morphological details of 2-D fibrous materials, including two dimensionless parameters (β and ζ). Next, we move on to establish an analytical fractal model for effective thermal conductivity.

2.3. Fractal of effective thermal conductivity

2.3.1. Thermal resistance of representative structure (RS)

The 2-D fibrous material considered in the current study is also thermally anisotropic, with heat flowing along mainly along in-plane and out-of-plane directions. Here, using the fractal theory and the technique of thermal-electrical analogy, we develop analytical models of effective thermal conductivity for both directions.

Consider the idealized topology of Fig. 1(f), and its representative structure (RS) illustrated in Fig. 3(a) and Fig. 4(a). In Figs. 3 and 4, λ represents the pore size of the RS, d_s denotes the thickness of each solid ligament, h is the height of the linked ligament in the z-direction, and b is the contact width of the linked ligament in the z-direction. The contact thermal resistance at the fiber interfaces makes the out-of-plane effective thermal conductivity less than the in-plane effective thermal conductivity under the same porosity. To consider the influence of contact thermal resistance on the model, a different ligament is introduced in the z-direction of the representative structure (see Fig. 1(f)). The contact thermal resistance of different metal fiber materials is quantified by different combinations of dimensionless parameters (β and ζ). The dimensionless parameters β and ζ correspond to geometric parameters b and h, respectively. The source literatures of the effective thermal conductivity experimental data also do not give specific methods for measuring or determining the contact thermal resistance at the fiber interfaces. In the current study, the model predictions are in good agreement with the experimental data by adjusting these two dimensionless parameters β and ζ. Therefore, the dimensionless parameters (β and ζ) can also be regarded as one of the fitting parameters. But they have physical meaning. In this paper, two dimensionless fitting parameters (β and ζ) with physical meaning are called hypothetical parameters.

(a) In-plane

With heat flow imposed on the left of the RS in Fig. 3(a), heat is conducted mainly along the x-axis with an in-plane effective thermal conductivity with negligible lateral contact thermal resistance [71]. Therefore, we only need to consider thermal resistance along the direction of heat flow (x-axis). Further, the effects of thermal radiation and convection are ignored.

Regarding Fig. 3(a), the equivalent thermal resistance R_A of the first layer (layer A) may be considered as the thermal resistance in parallel with R_{A1} and R_{A2}, namely:

$$\frac{1}{R_A} = \frac{1}{R_{A1}} + \frac{1}{R_{A2}} = \frac{k_f k_s d_s \lambda}{k_s \lambda + k_f d_s} + \frac{k_s d_s^2}{\lambda + d_s} \tag{39}$$

where k_f and k_s are the thermal conductivity of the liquid and solid phase, respectively. Similarly, the equivalent thermal resistance of layer B may be considered as the thermal resistance in parallel with R_{B1} and R_{B2}, where R_{B1} is composed of R_{B1-1} and R_{B1-2} in series and R_{B1-1} is given by:

$$R_{B1-1} = \frac{\lambda}{k_f h d_s} \tag{40}$$

Concerning Fig. 3(d), the equivalent thermal resistance R_{B1-2} of the part B1-2 in layer B may be considered as that associated with the parallel connection of R_{B1-2-1}, R_{B1-2-2} and R_{B1-2-3}. Therefore, R_{B1-2} can be obtained by:

$$\frac{1}{R_{B1-2}} = \frac{1}{R_{B1-2-1}} + \frac{1}{R_{B1-2-2}} + \frac{1}{R_{B1-2-3}} \tag{41}$$

where

$$R_{B1-2-1} = R_{B1-2-3} = \frac{2d_s}{k_f h(d_s - b)} \tag{42}$$

$$R_{B1-2-2} = \frac{d_s - b}{k_f h b} + \frac{b}{k_s h b} \tag{43}$$

Upon reorganizing, R_{B1-2} can be expressed as:

$$\frac{1}{R_{B1-2}} = \frac{k_f h(d_s - b)}{d_s} + \frac{k_s k_f h b}{k_s(d_s - b) + k_f b} \tag{44}$$

Since the thermal resistance R_{B1} of the part B1 in layer B is associated with the series connection of R_{B1-1} and R_{B1-2}, it can be calculated by:

$$R_{B1} = R_{B1-1} + R_{B1-2} \tag{45}$$

The thermal resistance R_{B2} is simply given by:

$$R_{B2} = \frac{\lambda + d_s}{k_f h \lambda} \tag{46}$$

With reference to Fig. 3(c), the equivalent thermal resistance R_B of layer B may be taken as that connected by R_{B1} and R_{B2} in parallel, so that:

$$\frac{1}{R_B} = \frac{1}{R_{B1}} + \frac{1}{R_{B2}} = \frac{k_f h \lambda}{\lambda + d_s} + \frac{k_f h d_s \left[k_s(d_s - b)^2 + k_s b d_s + k_f b(d_s - b)\right]}{k_s \left[\lambda b d_s + (d_s - b)\left(d_s^2 + \lambda d_s - \lambda b\right)\right] + k_f \left(b d_s^2 + \lambda b d_s - \lambda b^2\right)} \tag{47}$$

The total in-plane thermal resistance of the RS shown in Fig. 3(a) can thence be obtained as:

$$\frac{1}{R_{RS-in}} = \frac{1}{R_A} + \frac{1}{R_B} = \lambda \phi_{in} \tag{48}$$

where

$$\phi_{in} = \frac{k_f \zeta + k_s \gamma^2}{1 + \gamma} + \frac{k_f k_s \gamma}{k_s + k_f \gamma} + \frac{k_f \zeta \gamma \left[k_s(1 - \beta)^2 + k_s \beta + k_f \beta(1 - \beta)\right]}{k_s \left[(1 - \beta)(\gamma + 1) + \beta^2\right] + k_f \beta(\gamma + 1 - \beta)} \tag{49}$$

$$d_s = \gamma \lambda, \quad b = \beta d_s, \quad h = \zeta \lambda \tag{50}$$

b) Out-of-plane

To determine the out-of-plane effective thermal conductibity, it is assumed that heat flow is imposed on the top of the RS, as shown in Fig. 4(a), with negligible lateral contact thermal resistance [71]. Therefore, we only need to consider thermal resistance along the heat flow direction (z-axis). Further, we neglect the effects of thermal radiation and convection.

Concerning Fig. 4(a) and (b), the equivalent thermal resistance of layer A may be considered as that associated with the parallel connection of R_{A1} and R_{A2}, so that its thermal resistance R_A is given by:
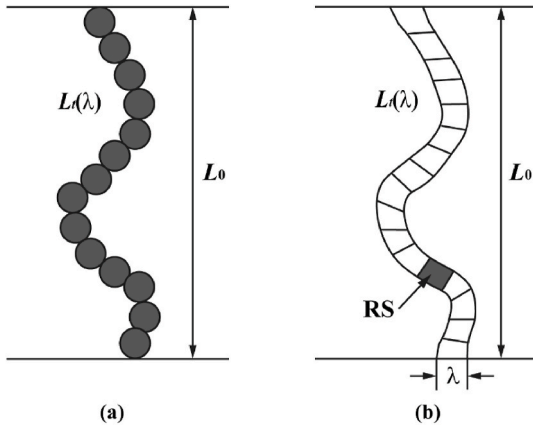
Fig. 5. Schematic of effective thermal conductivity for fibrous materials: (a) typical particle chain [29]; (b) fibrous material chain.
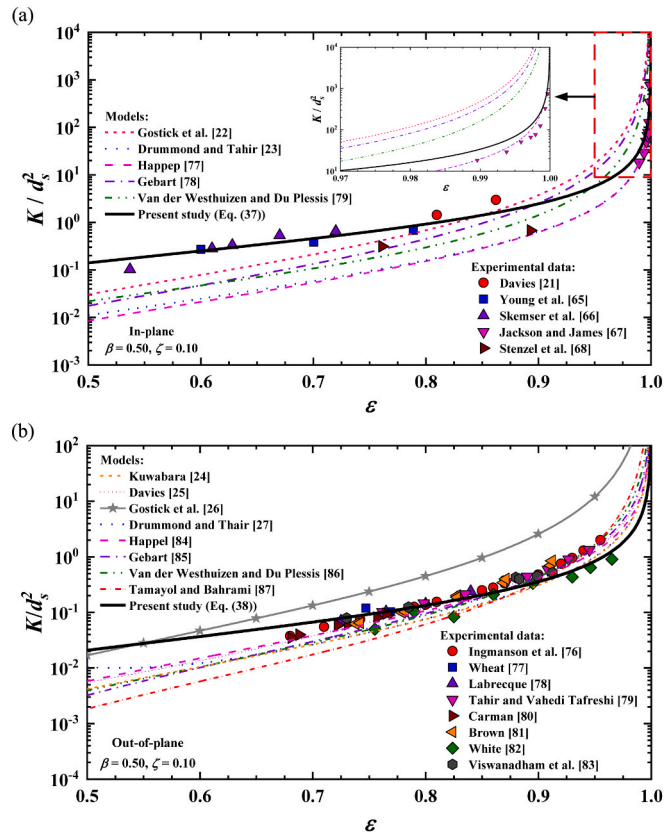

Fig. 6. Dimensionless permeability plotted as a function of porosity: (a) in-plane; (b) out-of-plane.

Fig. 7. Comparison of average RDs calculated with different values of dimensionless permeability: (a) in-plane; (b) out of plane.

$$\frac{1}{R_A} = \frac{1}{R_{A1}} + \frac{1}{R_{A2}} = \frac{k_f \lambda^2}{h + d_s} + \frac{k_s k_f \lambda d_s}{k_s h + k_f d_s} \tag{51}$$

Similarly, the equivalent thermal resistance R_{B1} of layer B may be taken as the thermal resistance in parallel with R_{B1} and R_{B2}, where R_{B2} consists of R_{B2-1} and R_{B2-2} in series, yielding:

$$R_{B1} = \frac{h}{k_f \lambda d_s} + \frac{d_s}{k_s \lambda d_s} \tag{52}$$

Other parts of the thermal resistance, such as R_{B2-1-1}, R_{B2-1-3}, $R_{B2-1-2-1}$, $R_{B2-1-2-2}$ and $R_{B2-1-2-3}$ can be calculated as:
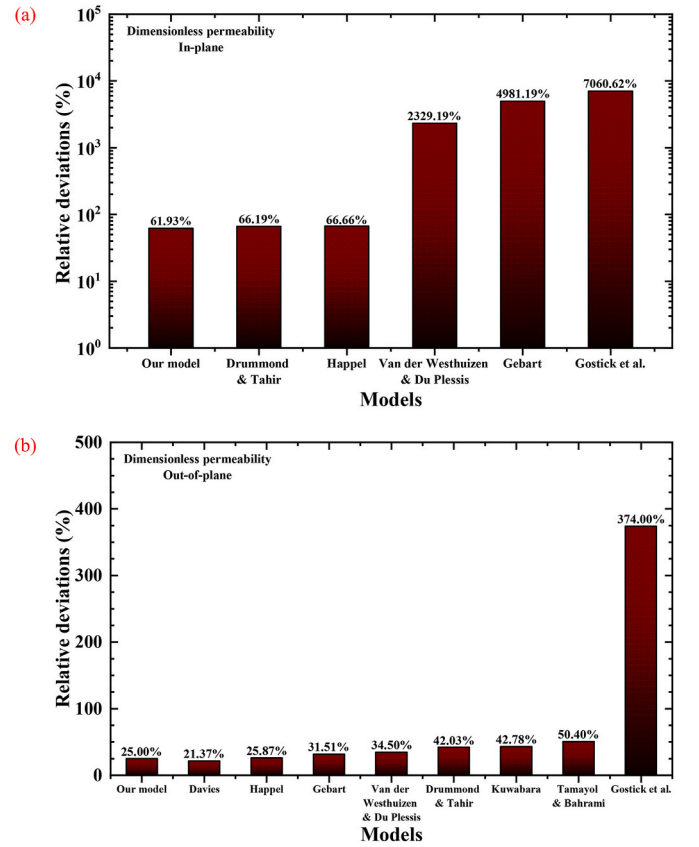
$$R_{B2-1-1} = R_{B2-1-3} = \frac{2h}{k_f d_s (d_s - b)} \tag{53}$$

$$R_{B2-1-2-1} = R_{B2-1-2-3} = \frac{2h}{k_f b (d_s - b)} \tag{54}$$

$$R_{B2-1-2-2} = \frac{h}{k_s b^2} \tag{55}$$

The equivalent thermal resistance $R_{B2\text{-}1\text{-}2}$ is composed of thermal resistance $R_{B2\text{-}1\text{-}2\text{-}1}$, $R_{B2\text{-}1\text{-}2\text{-}2}$ and $R_{B2\text{-}1\text{-}2\text{-}3}$ in parallel, namely:

$$\frac{1}{R_{B2-1-2}} = \frac{1}{R_{B2-1-2-1}} + \frac{1}{R_{B2-1-2-2}} + \frac{1}{R_{B2-1-2-3}} = \frac{k_f b(d_s - b)}{h} + \frac{k_s b^2}{h} \tag{56}$$

Similarly, the thermal resistance $R_{B2\text{-}1}$ is obtained by connecting $R_{B2\text{-}1\text{-}1}$, $R_{B2\text{-}1\text{-}2}$ and $R_{B2\text{-}1\text{-}3}$ in parallel:

$$\frac{1}{R_{B2-1}} = \frac{1}{R_{B2-1-1}} + \frac{1}{R_{B2-1-2}} + \frac{1}{R_{B2-1-3}} = \frac{k_f (d_s^2 - b^2)}{h} + \frac{k_s b^2}{h} \tag{57}$$

Hence, the equivalent thermal resistance $R_{B2\text{-}2}$ can be calculated by:

$$R_{B2-2} = \frac{d_s}{k_s d_s^2} \tag{58}$$

Since $R_{B2\text{-}1\text{-}}$ and $R_{B2\text{-}2}$ are connected in series to form the thermal resistance R_{B2} of the part B2 in layer B, it can be calculated as:

$$R_{B2} = R_{B2-1} + R_{B2-2} = \frac{h}{k_f (d_s^2 - b^2) + k_s b^2} + \frac{d_s}{k_s d_s^2} \tag{59}$$

It follows that the equivalent thermal resistance of layer B can be obtained as:

Table 1
Experimental data of permeability for fibrous materials.

References	Porosity, ε	K/d_s^2	d_s (mm)	Material	Direction
Davies [25]	0.862	2.975	N/A	N/A	In-plane
	0.810	1.438	N/A	N/A	
Young et al. [72]	0.600	0.271	N/A	N/A	In-plane
	0.700	0.383	N/A	N/A	
	0.789	0.676	N/A	N/A	
Skamser et al. [73]	0.537	0.102	0.01	Alumina fiber	In-plane
	0.610	0.282	0.01	Alumina fiber	
	0.628	0.329	0.01	Alumina fiber	
	0.670	0.533	0.01	Alumina fiber	
	0.720	0.648	0.01	Alumina fiber	
Jackson and James [74]	0.9896	18.5	9.8×10^{-7}	Hyaluronic acid polymer	In-plane
	0.99379	29.25	9.8×10^{-7}	Hyaluronic acid polymer	
	0.99586	51	9.8×10^{-7}	Hyaluronic acid polymer	
	0.99724	66.75	9.8×10^{-7}	Hyaluronic acid polymer	
	0.99793	77	9.8×10^{-7}	Hyaluronic acid polymer	
	0.99862	125	9.8×10^{-7}	Hyaluronic acid polymer	
	0.99931	332.5	9.8×10^{-7}	Hyaluronic acid polymer	
	0.999655	750	9.8×10^{-7}	Hyaluronic acid polymer	
Stenzel et al. [75]	0.761	0.3125	3.0×10^{-6}	Collagen	In-plane
	0.893	0.675	3.0×10^{-6}	Collagen	
Ingmanson et al. [76]	0.742	0.075	0.193	Nylon fibers	Out-of-plane
	0.768	0.0975	0.193	Nylon fibers	
	0.79	0.125	0.193	Nylon fibers	
	0.8	0.1375	0.193	Nylon fibers	
	0.83	0.2	0.193	Nylon fibers	
	0.85	0.2425	0.193	Nylon fibers	
	0.86	0.2775	0.193	Nylon fibers	
	0.87	0.3325	0.193	Nylon fibers	
	0.9	0.48	0.193	Nylon fibers	
	0.68	0.0375	0.164	Glass fibers	
	0.71	0.055	0.164	Glass fibers	
	0.81	0.155	0.164	Glass fibers	
	0.8	0.1375	0.164	Glass fibers	
	0.83	0.1975	0.164	Glass fibers	
	0.85	0.25	0.164	Glass fibers	
	0.87	0.375	0.164	Glass fibers	
	0.9	0.475	0.164	Glass fibers	
	0.91	0.625	0.164	Glass fibers	
	0.92	0.75	0.164	Glass fibers	
	0.93	0.95	0.164	Glass fibers	
	0.94	1.3	0.164	Glass fibers	
	0.955	2	0.164	Glass fibers	
Wheat [77]	0.747	0.11875	7.8×10^{-5}	Glass fibers	Out-of-plane
	0.769	0.103	1.44×10^{-4}	Glass fibers	
Labrecque [78]	0.725	0.07	0.0024	Nylon fibers	Out-of-plane
	0.765	0.1025	0.0024	Nylon fibers	
	0.8	0.1425	0.0024	Nylon fibers	
	0.84	0.2375	0.0024	Nylon fibers	
Tahir and Vahedi Tafreshi [79]	0.945	1.344	0.01	N/A	Out-of-plane
	0.927	0.903	0.01	N/A	
	0.908	0.588	0.01	N/A	
	0.890	0.445	0.01	N/A	
	0.872	0.357	0.01	N/A	
	0.835	0.213	0.01	N/A	
	0.799	0.147	0.01	N/A	
	0.762	0.103	0.01	N/A	
Carman [80]	0.681	0.035	0.328	Stainless steel wire crimps	Out-of-plane
	0.688	0.03975	0.328	Stainless steel wire crimps	
	0.722	0.0585	0.328	Stainless steel wire crimps	
	0.731	0.06125	0.328	Stainless steel wire crimps	
	0.757	0.0805	0.328	Stainless steel wire crimps	
	0.765	0.09475	0.328	Stainless steel wire crimps	

Table 1 (*continued*)

References	Porosity, ε	K/d_s^2	d_s (mm)	Material	Direction
Brown [81]	0.738	0.0625	0.072	Glass wool	Out-of-plane
	0.742	0.065	0.072	Glass wool	
	0.779	0.1	0.072	Glass wool	
	0.782	0.1025	0.072	Glass wool	
	0.828	0.2	0.072	Glass wool	
	0.828	0.1875	0.072	Glass wool	
	0.869	0.3425	0.072	Glass wool	
	0.871	0.4	0.072	Glass wool	
	0.911	0.7	0.072	Glass wool	
	0.912	0.85	0.072	Glass wool	
White [82]	0.755	0.05	7.0×10^{-7}	Acrylamide polymergel	Out-of-plane
	0.79	0.1025	7.0×10^{-7}	Acrylamide polymergel	
	0.825	0.0835	7.0×10^{-7}	Acrylamide polymergel	
	0.86	0.2095	7.0×10^{-7}	Acrylamide polymergel	
	0.895	0.3325	7.0×10^{-7}	Acrylamide polymergel	
	0.93	0.435	7.0×10^{-7}	Acrylamide polymergel	
	0.946	0.6425	7.0×10^{-7}	Acrylamide polymergel	
	0.965	0.905	7.0×10^{-7}	Acrylamide polymergel	
Viswanadham et al. [83]	0.73	0.079	3.01×10^{-6}	Collagen	Out-of-plane
	0.785	0.12375	2.90×10^{-6}	Collagen	
	0.88	0.4275	2.30×10^{-6}	Collagen	
	0.883	0.4	2.00×10^{-6}	Collagen	
	0.899	0.45	2.00×10^{-6}	Collagen	
	0.9125	0.52	2.00×10^{-6}	Collagen	

$$\frac{1}{R_B} = \frac{1}{R_{B1}} + \frac{1}{R_{B2}} = \frac{k_s k_f \lambda d_s}{k_s h + k_f d_s} + \frac{\left[k_f\left(d_s^2 - b^2\right) + k_s b^2\right] k_s d_s}{k_f\left(d_s^2 - b^2\right) + k_s\left(h d_s + b^2\right)} \tag{60}$$

Finally, the total out-of-plane thermal resistance of the RS shown in Fig. 4(a) is obtained as:

$$\frac{1}{R_{RS-out}} = \frac{1}{R_A} + \frac{1}{R_B} = \lambda \left\{ \frac{k_f}{\zeta + \gamma} + \frac{2 k_s k_f \gamma}{k_s \zeta + k_f \gamma} + \frac{k_s \gamma^2 \left[k_f\left(1 - \beta^2\right) + k_s \beta^2\right]}{k_f \gamma\left(1 - \beta^2\right) + k_s\left(\zeta + \gamma \beta^2\right)} \right\} = \lambda \phi_{out} \tag{61}$$

where

$$\phi_{out} = \frac{k_f}{\zeta + \gamma} + \frac{2 k_s k_f \gamma}{k_s \zeta + k_f \gamma} + \frac{k_s \gamma^2 \left[k_f\left(1 - \beta^2\right) + k_s \beta^2\right]}{k_f \gamma\left(1 - \beta^2\right) + k_s\left(\zeta + \gamma \beta^2\right)} \tag{62}$$

$$d_s = \gamma \lambda, \quad b = \beta d_s, \quad h = \zeta \lambda \tag{63}$$

2.3.2. The RS chain model

With heat conduction paths described as multiple tortuous heat chains in parallel, previous research has established an analytical thermal conductivity model for particulate porous media [29]. Each chain was consisted of particles in close contact, as shown in Fig. 5(a). Built upon this theoretical concept, for the present idealized topological structure of 2-D fibrous materials (Fig. 3 and 4), heat conduction along randomly-distributed RSs in close contact, as shown in Fig. 5(b), may be treated as heat flow along multiple RS chains in parallel. We first use the series model to derive the effective thermal conductivity of a single RS chain, and then use the parallel model to derive the effective conductivity of the 2-D fibrous material consisted of multiple RS chains having different pore sizes.

Since fibrous materials are typically anisotropic, we mainly consider in-plane and out-of-plane effective thermal conductivities, assuming the curved RS chains obey the fractal distribution law in both directions.

a) In-plane

As a curved chain with the length of $L_t(\lambda) = \lambda^{1-D_T} L_0^{D_T}$ contains a number of $L_t(\lambda)/(a + d_s)$ RSs in the in-plane direction, applying the Fourier law of heat conduction dictates that the in-plane thermal resistance is given by:

$$R_{chain-in} = \frac{L_t(\lambda)}{\lambda + d_s} R_{RS-in} = \frac{\lambda^{-1-D_T} L_0^{D_T}}{1 + \gamma} \phi_{in}^{-1} \tag{64}$$

Within the infinitesimal range from λ to $\lambda + d\lambda$ for pore sizes, the number of curved chains is $-dN$. These chains are connected in parallel so that their total in-plane thermal resistance R_{t-in} is calculated as:

$$\frac{1}{R_{t-in}} = \int_{\lambda_{min}}^{\lambda_{max}} \frac{D_{f,2} \lambda_{max}^{D_f} \lambda^{-(D_{f,2}+1)} d\lambda}{R_{chain-in}} = \frac{(1+\gamma) D_{f,2} \lambda_{max}^{1+D_T}}{L_0^{D_T}\left(1 + D_T - D_{f,2}\right)} \left(1 - \varepsilon^{\frac{1+D_T-D_{f,2}}{2-D_{f,2}}}\right) \phi_{in} \tag{65}$$

b) Out-of-plane

Similarly, given that a curved chain with the length of $L_t(\lambda) = \lambda^{1-D_T} L_0^{D_T}$ contains a number of $L_t(\lambda)/(h + d_s)$ RSs in the out-of-plane direction, its out-of-plane thermal resistance is:

Table 2
Relative deviations (RDs) between dimensionless permeability and experimental data for fibrous materials.

| Direction	Model	RD range	Average RD
In-plane	Present study	3.78–233.93%	61.93%
	Gostick et al. [26]	12.51–53979.38%	7060.62%
	Drummond and Tahir [27]	1.04–91.64%	66.19%
	Happel [84]	0.27–92.46%	66.66%
	Gebart [85]	13.37–38050.63%	4981.19%
	Van der Westhuizen and Du Plessis [86]	38.20–17703.60%	2329.82%
Out-of-plane	Present study	0.18–96.82%	25.00%
	Kuwabara [24]	7.95–86.68%	42.78%
	Davies [25]	1.49–163.04%	21.37%
	Gostick et al. [26]	92.70–2760.67%	373.98%
	Drummond and Tahir [27]	7.59–91.80%	42.03%
	Happel [84]	1.27–132.33%	25.87%
	Gebart [85]	4.17–198.43%	31.51%
	Van der Westhuizen and Du Plessis [86]	0.44–252.17%	34.50%
	Tamayol and Bahrami [87]	2.16–300.37%	50.40%
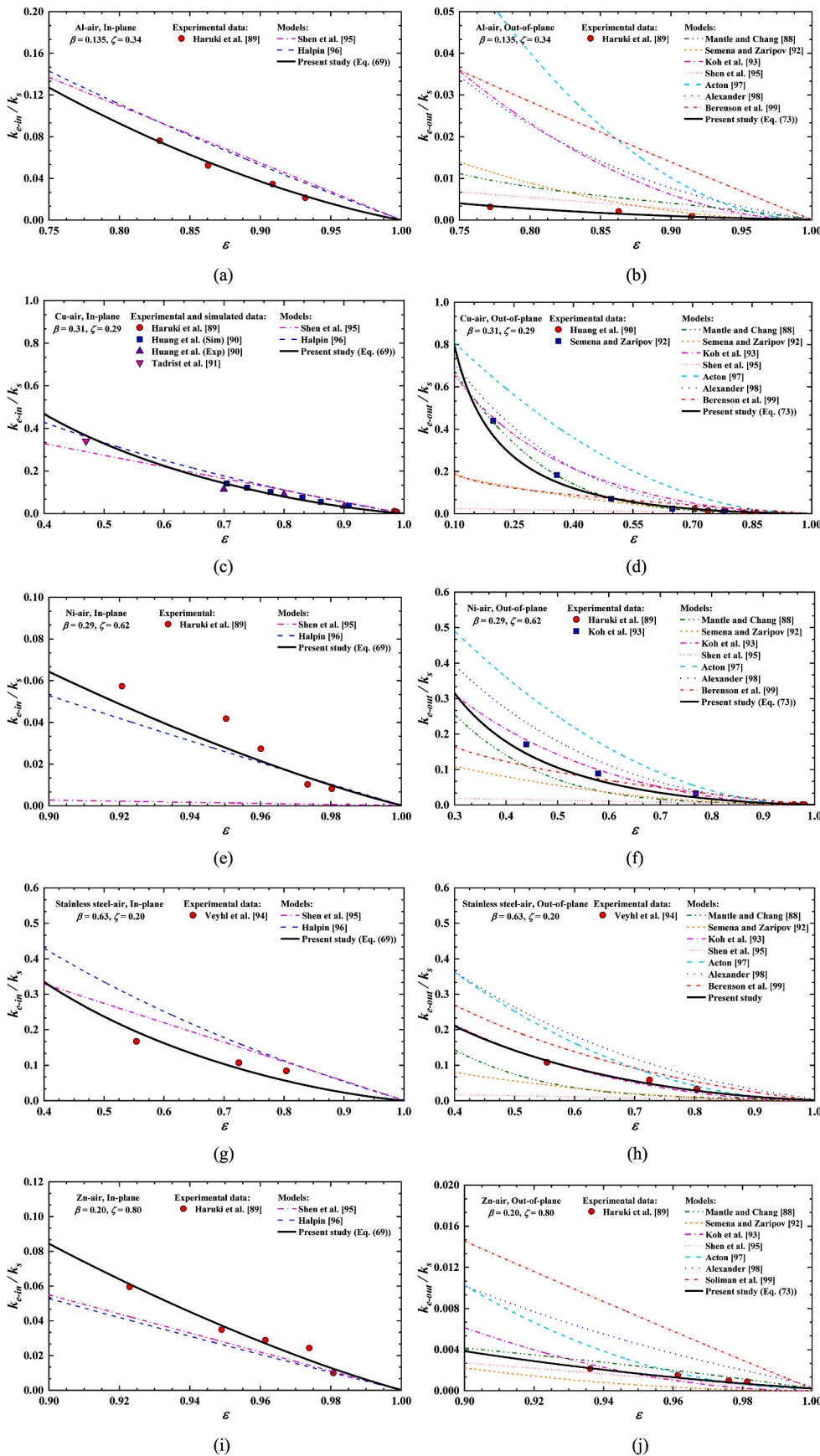
Fig. 8. Comparisons between predictions obtained with effective thermal conductivity models and open literature data for air-saturated metallic fibrous materials: (a) in-plane effective and (b) out-of-plane effective conductivity of air-saturated Al (aluminum) fibers; (c) in-plane and (d) out-of-plane effective conductivity of air-saturated Cu (copper) fibers; (e) in-plane and (f) out-of-plane effective conductivity of air-saturated Ni (nickel) fibers; (g) in-plane and (h) out-of-plane effective conductivity of air-saturated stainless steel fibers; (i) in-plane and (j) out-of-plane effective conductivity of air-saturated Zn (zinc) fibers.

Table 3

Thermal conductivities of materials makes used for analytical model predictions.

Material	k (W/(m-K))	Material	k (W/(m-K))
Aluminum	203	Stainless steel	14.8
Copper	398	Zinc	121
Nickle	91.4	Air	0.026

Table 4

Experimental and simulation data of effective thermal conductivity for air-saturated metallic fibrous materials (Al, Cu, Ni, Steel, Zn).

References	Porosity, ε	k_e/k_s	Remark
Harukai et al. [89]	0.829	0.0760	Al-air (In-plane)
	0.863	0.0523	
	0.909	0.0345	
	0.932	0.0213	
Harukai et al. [89]	0.772	0.0031	Al-air (Out-of-plane)
	0.863	0.0021	
	0.915	0.0010	
Harukai et al. [89]	0.984	0.0105	Cu-air (In-plane)
	0.988	0.0075	
Harukai et al. [89]	0.921	0.0574	Ni-air (In-plane)
	0.950	0.0417	
	0.960	0.0273	
	0.973	0.0102	
	0.980	0.0081	
Harukai et al. [89]	0.934	0.0019	Ni-air (Out-of-plane)
	0.960	0.0013	
	0.976	0.0010	
	0.981	0.0008	
Harukai et al. [89]	0.923	0.0595	Zn-air (In-plane)
	0.949	0.0348	
	0.962	0.0288	
	0.974	0.0243	
	0.981	0.0099	
Harukai et al. [89]	0.936	0.0021	Zn-air (Out-of-plane)
	0.961	0.0015	
	0.976	0.0010	
	0.981	0.0009	
Huang et al. [90]	0.908	0.0360	Cu-air (In-plane)
	0.861	0.0546	
	0.831	0.0750	
	0.778	0.1004	
	0.739	0.1211	
	0.705	0.1406	
	0.900	0.0343	
	0.800	0.0889	
	0.700	0.1135	
Huang et al. [90]	0.908	0.0008	Cu-air (Out-of-plane)
	0.861	0.0017	
	0.831	0.0038	
	0.778	0.0085	
	0.739	0.0140	
	0.705	0.0229	
Tadrist et al. [91]	0.470	0.340	Cu-air (In-plane)
Semena and Zaripov [92]	0.198	0.4395	Cu-air (Out-of-plane)
	0.359	0.1835	
	0.495	0.0836	
	0.649	0.0245	
	0.781	0.0121	
Koh et al. [93]	0.440	0.1709	Ni-air (Out-of-plane)
	0.579	0.0889	
	0.769	0.0328	
Veyhl et al. [94]	0.804	0.0841	Steel-air (In-plane)
	0.725	0.107	
	0.554	0.167	
Veyhl et al. [94]	0.804	0.0332	Steel-air (Out-of-plane)
	0.725	0.0580	
	0.554	0.1080	

Table 5

The Mean Squared Error results between effective conductivity models and experimental data.

Models	Al-air	Cu-air	Ni-air	Steel-air	Zn-air	Direction
Shen et al. [95]	91.212	109.057	9.197	0.631	1.467	In-plane
Halpin [96]	11.763	113.547	0.949	1.344	1.890	
Present study	0.176	25.651	0.549	0.131	0.197	
Mantle and Chang [88]	0.808	3.397	8.015	0.407	0.003	Out-of-plane
Semena and Zaripov [92]	1.039	1398.859	15.657	0.465	0.016	
Koh et al. [93]	11.165	184.987	0.326	0.026	0.005	
Shen et al. [95]	0.187	2989.596	36.956	0.904	0.002	
Acton [97]	37.449	2091.687	34.348	0.667	0.018	
Alexander [98]	10.961	204.085	6.131	1.130	0.078	
Berenson et al. [99]	17.565	1469.456	4.828	0.292	0.286	
Present study	0.006	91.606	1.402	0.011	0.001	

$$R_{chain-out} = \frac{L_t(\lambda)}{h+d_s} R_{RS-out} = \frac{\lambda^{-1-D_T} L_0^{D_T}}{\zeta+\gamma} \phi_{out}^{-1} \tag{66}$$

Within the infinitesimal range from λ to $\lambda + d\lambda$ for pore sizes, the number of curved chains is $-dN$. These chains are also connected in parallel so that their total out-of-plane thermal resistance R_{t-out} becomes:

$$\frac{1}{R_{t-out}} = \int_{\lambda_{min}}^{\lambda_{max}} \frac{D_{f,2}\lambda_{max}^{D_f} \lambda^{-(D_{f,2}+1)} d\lambda}{R_{chain-out}} = \frac{(\zeta+\gamma)D_{f,2}\lambda_{max}^{1+D_T}}{L_0^{D_T}(1+D_T-D_{f,2})} \left(1 - \varepsilon^{\frac{1+D_T-D_{f,2}}{2-D_{f,2}}}\right) \phi_{out} \tag{67}$$

2.3.3. The effective thermal conductivity

a) In-plane

The in-plane effective thermal conductivity can be calculated as $k_{e-in} = \frac{L_0}{A_{in}R_{t-in}}$. According to Eqs. (12), (13) and (65), the in-plane effective thermal conductivity is then given by:

$$k_{e-in} = \frac{4(1+\gamma)(2-D_{f,2})\varepsilon}{\zeta\pi(1+D_T-D_{f,2})(1-\varepsilon)} \left[\frac{\pi D_{f,3}}{6(3-D_{f,3})} \frac{(1-\varepsilon)}{\varepsilon}\right]^{\frac{1-D_T}{3}} \left(1 - \varepsilon^{\frac{1+D_T-D_{f,2}}{2-D_{f,2}}}\right) \phi_{in} \tag{68}$$

or, expressed in dimensionless form:

$$\frac{k_{e-in}}{k_s} = \frac{4(1+\gamma)(2-D_{f,2})\varepsilon}{\zeta\pi(1+D_T-D_{f,2})(1-\varepsilon)} \left[\frac{\pi D_{f,3}}{6(3-D_{f,3})} \frac{(1-\varepsilon)}{\varepsilon}\right]^{\frac{1-D_T}{3}} \left(1 - \varepsilon^{\frac{1+D_T-D_{f,2}}{2-D_{f,2}}}\right) \phi_{in}^{+} \tag{69}$$

where

$$\phi_{in}^{+} = \frac{k^+\zeta+\gamma^2}{1+\gamma} + \frac{k^+\gamma}{1+k^+\gamma} + \frac{k^+\zeta\gamma[(1-\beta)^2+\beta+k^+\beta(1-\beta)]}{(1-\beta)(\gamma+1)+\beta^2+k^+\beta(\gamma+1-\alpha\beta)} \tag{70}$$

$$k^+ = k_f/k_s \tag{71}$$

(a) Out-of-plane

With the out-of-plane effective thermal conductivity given by $k_{e-out} = \frac{L_0}{A_{out}R_{t-out}}$, from Eqs. (12), (15) and (67) we arrive at:

$$k_{e-out} = \frac{(\zeta+\gamma)(2-D_{f,2})\varepsilon}{(1+D_T-D_{f,2})(1-\varepsilon)} \left[\frac{\pi D_{f,3}}{6(3-D_{f,3})} \frac{(1-\varepsilon)}{\varepsilon}\right]^{\frac{1-D_T}{3}} \left(1 - \varepsilon^{\frac{1+D_T-D_{f,2}}{2-D_{f,2}}}\right) \phi_{out} \tag{72}$$

Table 6

Relative deviations (RDs) between effective conductivity models and experimental data for air-saturated metallic fibrous materials.

| Sample	Model	RD range	Average RD	Direction
Al-air	Present study	1.25–8.28%	5.02%	In-plane
	Shen et al. [95]	91.33–93.90%	92.74%	
	Halpin [96]	23.22–65.68%	42.07%	
Cu-air	Present study	0.96–65.92%	20.14%	In-plane
	Shen et al. [95]	11.85–59.79%	27.31%	
	Halpin [96]	6.06–55.56%	28.95%	
Ni-air	Present study	15.90–33.64%	25.08%	In-plane
	Shen et al. [95]	92.21–96.66%	94.65%	
	Halpin [96]	24.28–37.89%	30.98%	
Steel-air	Present study	15.35–33.36%	21.68%	In-plane
	Shen et al. [95]	28.83–46.68%	39.03%	
	Halpin [96]	31.25–72.82%	51.55%	
Zn-air	Present study	2.70–28.85%	14.00%	In-plane
	Shen et al. [95]	6.51–40.85%	24.58%	
	Halpin [96]	1.05–44.97%	26.93%	
Al-air	Present study	5.61–17.85%	13.02%	Out-of-plane
	Mantle and Chang [88]	156.64–268.61%	209.96%	
	Semena and Zaripov [92]	66.34–267.53%	144.83%	
	Koh et al. [93]	363.70–850.87%	551.81%	
	Shen et al. [95]	78.43–138.87%	104.51%	
	Acton [97]	663.20–1557.93%	1010.26%	
	Alexander [98]	488.22–821.40%	616.51%	
	Berenson et al. [99]	823.32–1123.28%	961.00%	
Cu-air	Present study	1.65–281.84%	74.82%	Out-of-plane
	Mantle and Chang [88]	1.48–340.58%	66.02%	
	Semena and Zaripov [92]	8.41–153.67%	51.90%	
	Koh et al. [93]	363.70–850.87%	217.99%	
	Shen et al. [95]	20.00–194.17%	78.30%	
	Acton [97]	46.36–1045.35%	493.95%	
	Alexander [98]	13.39–458.02%	160.24%	
	Berenson et al. [99]	13.10–1363.01%	340.33%	
Ni-air	Present study	15.05–90.06%	38.80%	Out-of-plane
	Mantle and Chang [88]	36.34–69.59%	53.36%	
	Semena and Zaripov [92]	48.54–89.71%	68.07%	
	Koh et al. [93]	6.53–69.71%	31.99%	
	Shen et al. [95]	4.98–91.14%	49.71%	
	Acton [97]	12.91–148.32%	67.49%	
	Alexander [98]	23.76–286.02%	144.60%	
	Berenson et al. [99]	11.64–423.51%	199.54%	
Steel-air	Present study	4.38–17.69%	12.23%	Out-of-plane
	Mantle and Chang [88]	52.53–73.30%	65.47%	
	Semena and Zaripov [92]	59.04–74.27%	68.10%	
	Koh et al. [93]	3.99–32.62%	20.86%	
	Shen et al. [95]	82.59–88.42%	85.82%	
	Mantle and Chang [88]	52.53–73.30%	65.47%	
	Acton [97]	22.46–86.29%	47.71%	
	Alexander [98]	81.00–102.66%	95.18%	
	Berenson et al. [99]	41.03–60.43%	50.81%	
Zn-air	Present study	2.53–23.47%	11.81%	Out-of-plane
	Mantle and Chang [88]	25.84–35.91%	33.27%	
	Semena and Zaripov [92]	57.48–90.87%	74.06%	
	Koh et al. [93]	20.41–73.13%	39.28%	
	Shen et al. [95]	18.17–35.70%	25.38%	
	Acton [97]	15.00–102.38%	45.17%	
	Alexander [98]	119.42–176.55%	148.53%	
	Berenson et al. [99]	222.33–331.99%	288.25%	
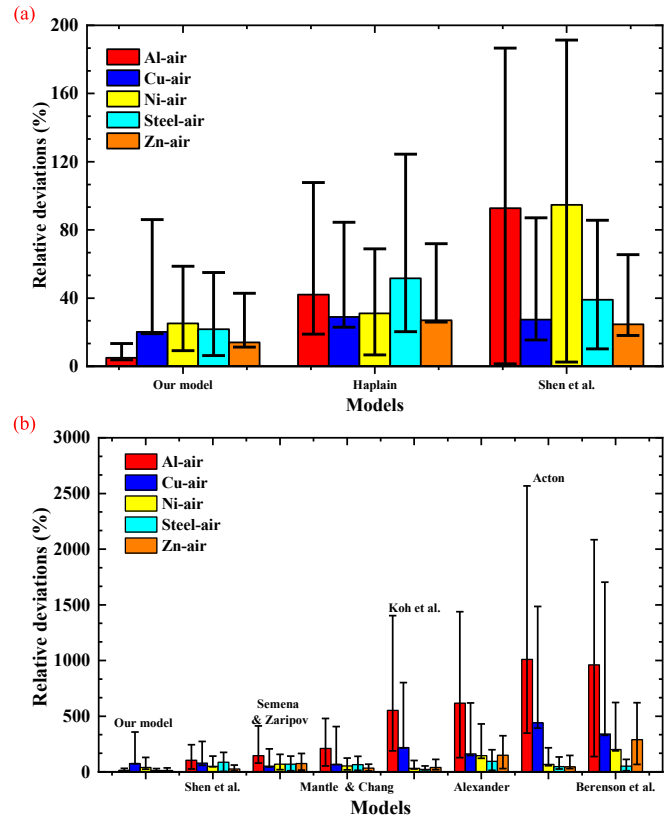
Fig. 9. Comparison of RDs for metallic fibrous materials and different models: (a) in-plane; (b) out-of-plane.

Rearranging, we have:

$$\frac{k_{e-out}}{k_s} = \frac{(\zeta+\gamma)(2-D_{f,2})\varepsilon}{(1+D_T-D_{f,2})(1-\varepsilon)}\left[\frac{\pi D_{f,3}}{6(3-D_{f,3})}\frac{(1-\varepsilon)}{\varepsilon}\right]^{\frac{1-D_T}{3}}\left(1-\varepsilon^{\frac{1+D_T-D_{f,2}}{2-D_{f,2}}}\right)\phi_{out}^+ \tag{73}$$

where

$$\phi_{out}^+ = \frac{k^+}{\zeta+\gamma} + \frac{2k^+\gamma}{\zeta+k^+\gamma} + \frac{\gamma^2\left[k^+\left(1-\beta^2\right)+\beta^2\right]}{k^+\gamma\left(1-\beta^2\right)+\left(\zeta+\gamma\beta^2\right)} \tag{74}$$

3. Results and discussion

3.1. Permeability as a function of porosity

For validation, predictions of the present analytical fractal model are compared with not only existing experimental data [25,72–83], but also predictions obtained using alternative analytical models proposed by others [24–27,84–87]. Comparison of the present model predictions and experimental data is presented in Fig. 6, where it is seen that the dimensionless permeability always increases with increasing porosity. When the porosity increases, the percentage of fibers (solid ligaments) decreases if the volume of fibrous material remains fixed. Thus, the obstruction effect of the solid on fluid flow is reduced. Fig. 6(a) and (b) display separately the in-plane and out-of-plane dimensionless permeability. By comparing with alternative permeability models, we note that predictions of the present fractal model are in good agreement with experimental data over the whole range of porosity considered. For example, in the high porosity range of $0.95 < \varepsilon < 1.00$, the Happel model, the Drummond-Tahir model and the present model are in good agreement with experimental data for in-plane dimensionless permeability (Fig. 6(a)), while other models always overestimate. At smaller
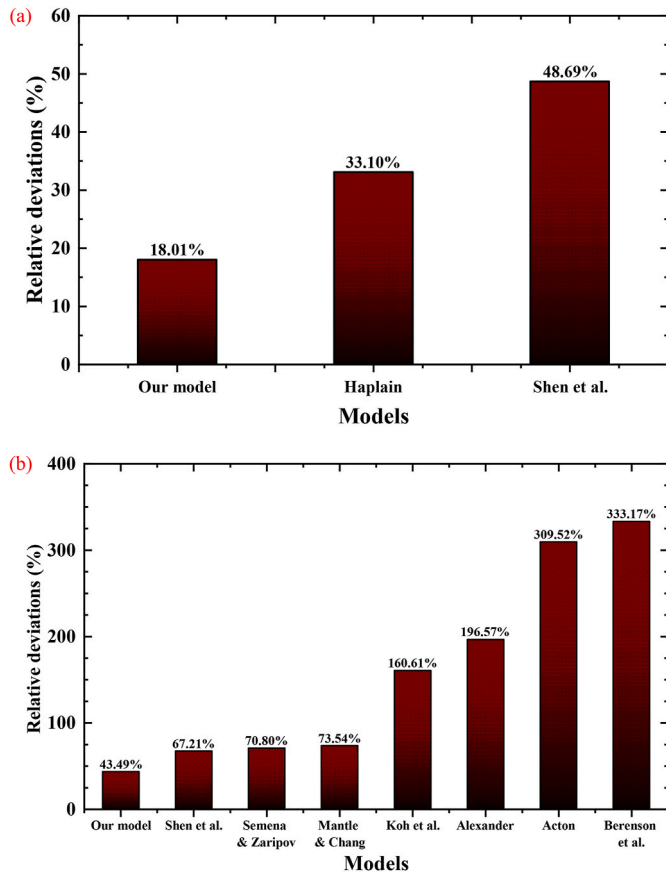
Fig. 10. Comparison of average RDs calculated with different effective conductivity models for air-saturated metallic fibrous materials: (a) in-plane; (b) out-of-plane.

porosity levels ($0.50 < \varepsilon < 0.80$), the present model can also accurately predict the experimentally measured variation trend of in-plane dimensionless permeability with porosity, while other models always underestimate as shown in Fig. 6(a). As for the out-of-plane dimensionless permeability, while the model of Gostick et al. consistently overestimates, predictions obtained using the remaining models agree quite well with experimental data (in Fig. 6(b)).

For quantitative comparison, relative deviation (*RD*) is applied to evaluate different permeability models, defined by:

$$RD = \left| \frac{\left(\frac{K}{d_s^2}\right)_{pre} - \left(\frac{K}{d_s^2}\right)_{exp}}{\left(\frac{K}{d_s^2}\right)_{exp}} \right| \qquad (75)$$

where the subscripts "exp" and "pre" denote separately experimental measurements and analytical model predictions (see Table 1).

Upon averaging all the RD values for each analytical model, Fig. 7 compares the average RDs calculated with different models. Apparently, with an average deviation of 61.93%, our model of in-plane permeability presents the smallest RD among all the models considered, followed by the model of the Drummond-Tahir model (66.19%), the Happel model (66.66%), the Van der Westhuizen-Du Plessis model (2329.19%), the Gebart model (4918.19%), and the Gostick et al. (7060.62%). As for the out-of-plane permeability, the average deviation of our model is 25.00%, followed by the Davies model (21.37%), the Happel model (25.87%), the Gebart model (31.51%), the Van der Westhuizen-Du Plessis model (34.50%), the Drummond-Tahir model (42.03%), the Kuwarbara model (42.78%), the Tamayol and Bahrami model (50.40%), and the Gostick et al. model (374.00%). Note that, while the average deviation of the Davies model is the smallest among these models for out-of-plane dimensionless permeability, the model did not consider in-plane permeability model for fibrous materials. The results show that the present fractal model can give better predictions of dimensionless permeability compared to other models. More detailed relative deviation results on dimensionless permeability are listed in Table 2 to further compare the present model with alternative analytical models. It should be noted here that the experimental data for fibrous porous media permeability have strong diversity and divergence, since they are measured based on different kinds of fibrous porous media with various pore shapes and diameter distributions. Therefore, the permeability predicted by the models will bring huge deviation due to individual data points. It is inadequate to judge a model only according to RD and average RD (see Table 2). One should select a proper model according to the specific porosity range when predicting permeability.

The permeability model developed in this study on the basis of fractal theory applies to fibers with random in-plane fiber orientation, because random size and distribution of the pores is the starting point of the fractal theory. Specifically, the analytical permeability model of Eqs. (37) and (38) is mainly related to the fractal dimension of pore distribution D_f, the fractal dimension of average tortuosity D_T, the porosity ε, the pore size ratio $\lambda_{min}/\lambda_{max}$, and the geometric parameters γ, β and ζ.

3.2. Effective thermal conductivity

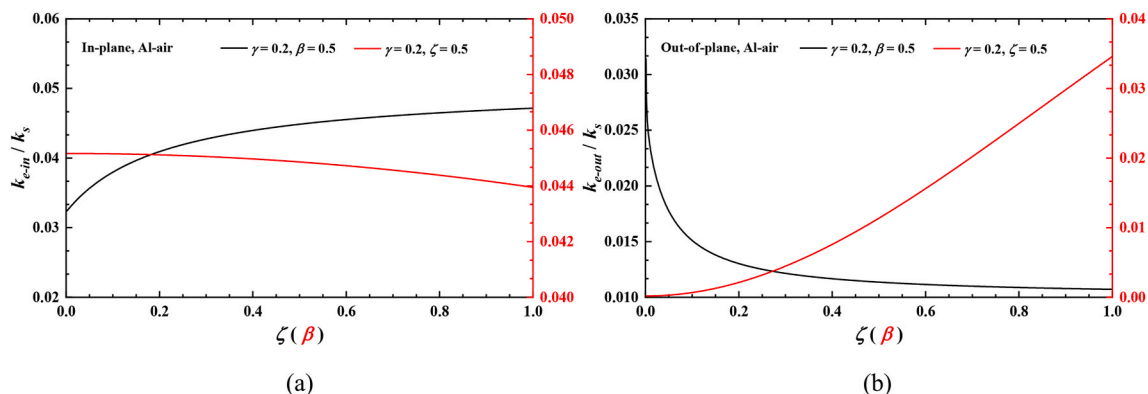For air-saturated metallic fibrous materials, Fig. 8 compares the

Fig. 11. Dimensionless effective thermal conductivity plotted as a function of ζ and β for selected values of γ: (a) in-plane; (b) out-of-plane.
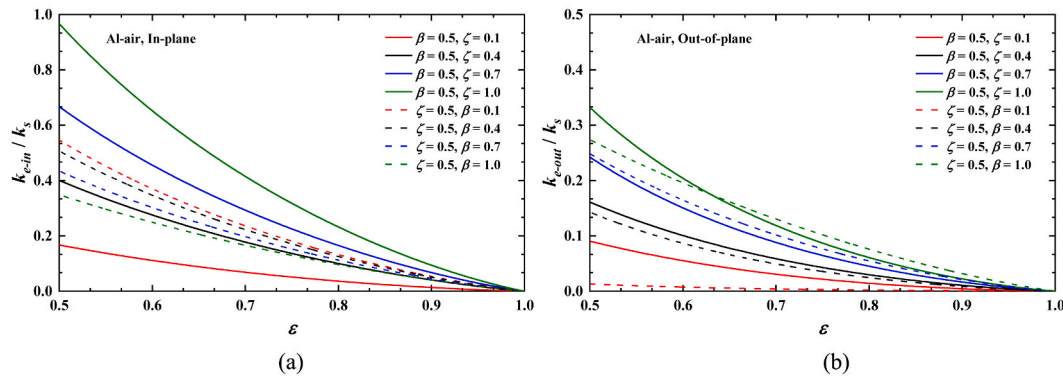
Fig. 12. Dimensionless effective thermal conductivity plotted as a function of porosity for selected values of dimensionless parameters β and ζ: (a) in-plane; (b) out-of-plane.

predictions of effective thermal conductivity obtained from both the current model and existing models, as well as the available experimental and simulated data (also listed in Table 4). The analytical model predictions are developed using material properties of Table 3. As seen, while the effective thermal conductivity decreases with increasing porosity, at high porosities ($\varepsilon > 0.75$), it decreases almost linearly with porosity. For fibrous materials made of different parent materials (aluminum, copper, or nickel), predictions of the present fractal model are in fairly good agreement with experimental and simulated data as manifested in Fig. 8. For the in-plane effective conductivity of air-saturated Al and Stainless steel fibrous materials, the Haplain model and the Shen et al. model both overestimate, as shown in Fig. 8(a) and (g). In contrast, for the in-plane effective conductivity of Ni and Zn fibrous materials saturated with air, the Haplain model and the Shen et al. model both significantly underpredict, as shown in Fig. 8(e) and (i)). For Cu fibers saturated with air, the two models predicted relatively better; Fig. 8(c). Regardless of material make (Al, Ni, Cu, stainless steel, or Zn), predictions of the Acton model and the Alexander model always overestimate the effective out-of-plane conductivity, while the model of Shen et al. always underestimates when the porosity is less than 0.9, as shown in Fig. 8(b), (d), (f), (h) and (j)). According to Fig. 8(b), the present model predictions are in good agreement with experimental data, while the alternative models tend to overpredict. The model proposed by Mantle and Chang [88] can correctly predict the trend of out-of-plane effective conductivity with porosity for Cu fibers, as shown in Fig. 8(d). Moreover, as per Fig. 8(f) and (h), the Koh et al. model can accurately predict the trend of out-of-plane effective conductivity.

In Fig. 8, at fixed porosity, the in-plane effective conductivity of a given fibrous material is generally larger than the out-of-plane effective conductivity. The main reason is that the former is mainly along the direction of in-plane fibers, while the latter is mainly influenced by the contact thermal resistance of fiber layers and the air layer between fiber gaps.

To assess the precision of different effective conductivity models, two systems are applied, namely, the Mean Square Error (MSE) system and the relative deviations (RDs) system. The MSE results are summarized in Table 5. The overall MSE values of our fractal model are relatively low. For in-plane effective conductivity, our model achieves the lowest MES. For the out-of-plane effective conductivity excluding Cu-air, our model also has low MES values (see Table 6).

Fig. 9 (a) and (b) present separately the RD values of in-plane and out-of-plane effective conductivity for different models. Upon averaging all the *RD* values for each model, Fig. 10 compares the average *RDs* calculated with different models. For in-plane effective conductivity, with an average deviation of 18.01%, our model presents the lowest RD value, followed by the Haplin model (33.10%) and the Shen et al. model (48.69%). For out-of-plane effective conductivity, with an average deviation of 43.49%, our model also presents the lowest RD value,

followed by the Shen et al. model (67.21%), the Semena-Zaripov model (70.80%), the Mantle-Chang model (73.54%), the Koh et al. model (160.61%), the Alexander model (196.57%), the Acton model (309.52%), and the Berenson et al. model (333.17%). The results clearly show that, compared to existing models, our model can provide better predictions of effective thermal conductivity for metallic fibrous materials.

Fig. 11 demonstrates how the dimensionless effective thermal conductivity varies with dimensionless parameters γ, β and ζ. In Fig. 11(a), the in-plane effective conductivity is seen to increase with increasing ζ when $\gamma = 0.2$ and $\beta = 0.5$, but the in-plane conductivity slightly decreases with increasing β when $\gamma = 0.2$ and $\zeta = 0.5$. When $0 < \zeta < 0.2$, the in-plane conductivity sharply increases with ζ. Further, when $0.2 < \zeta < 1.0$, the dimensionless in-plane conductivity steadily increases with ζ. The main factor affecting the in-plane conductivity is the thermal conductivity along fibers. In Fig. 11(b), the out-of-plane conductivity decreases with ζ when $\gamma = 0.2$ and $\beta = 0.5$, but increases with β when $\gamma = 0.2$ and $\zeta = 0.5$. The out-of-plane conductivity sharply decreases with ζ when $0 < \zeta < 0.2$, and slightly decreases with ζ when $0.2 < \zeta < 1.0$. The out-of-plane conductivity is mainly affected by the contact thermal resistance caused by different fiber layers. With γ and β both fixed, the value of ζ indicates the spacing between fiber layers. Thus, the out-of-plane effective thermal conductivity is reduced as ζ is increased.

Fig. 12 shows the variation of dimensionless effective thermal conductivity with porosity for different dimensionless parameters. In Fig. 12 (a), when $\beta = 0.5$, the in-plane conductivity increases with ζ at the same porosity; when $\zeta = 0.5$, the in-plane conductivity decreases with β at the same porosity. In Fig. 12(b), the out-of-plane conductivity increases with ζ for the same porosity when $\beta = 0.5$, and the situation is similar when $\zeta = 0.5$. When β is increased, the original porosity is reduced. Thus, to maintain a constant porosity, γ needs to be reduced accordingly. As the main influencing factor for in-plane conductivity is γ, it decreases when γ is decreased as shown in Fig. 12(a). Further, as shown in Fig. 12 (b), as the out-of-plane conductivity is mainly affected by β, it increases with increasing β.

For a 2-D fibrous material, different values of γ, β, and ζ correspond to different morphological structures. Here, ζ indicates the spacing between fiber layers while γ denotes the fiber percentage in the pore. That is, when γ is increased, the fiber diameter is larger at the same pore size and heat conduction along the fiber is stronger. Fiber contact area (when different fiber layers overlap) is represented by β. A higher β means that the fibers of different fiber layers have a larger contact area with each other, and hence the thermal contact resistance between fibers is reduced. The out-of-plane effective conductivity is mainly influenced by thermal contact resistance between fibers, thus β is the dominant influencing factor.

4. Conclusions

The fractal theory has been used to first characterize randomly-distributed pores in a 2-D fibrous material and then develop analytical models for predicting its permeability and effective thermal conductivity, for both in-plane and out-of-plane directions. The permeability is analytically expressed as a function of porosity, average tortuosity, pore size distribution, and fractal dimension. The effective thermal conductivity is analytically expressed as a function of porosity, thermal conductivity of the solid and filling medium, average tortuosity, pore size distribution, and fractal dimension. In contrast to previous permeability models and effective conductivity models, the present models contain two hypothetical parameters (β and ζ) with physical meaning to consider the contact thermal resistance. The model predictions of permeability compare well with existing experimental data for fibrous metallic materials over a wide range of porosity (from 0.50 to 0.99). Relative to existing analytical models, the present fractal model exhibits the smallest relative deviations from experimental data, 61.93% and 25.00% for in-plane and out-of-plane directions, respectively. Similarly, compared with existing effective conductivity models, the present model exhibits good accuracy (relative deviation 18.01% and 43.49% from experimental data for in-plane and out-of-plane directions, respectively) for aluminum, copper, nickel, stainless steel and zinc fibrous materials saturated with air.

Declaration of competing interest

The authors declare that they have no known competing financial interests or personal relationships that could have appeared to influence the work reported in this paper.

Data availability

Data will be made available on request.

Acknowledgements

References

[1] A. Tamayol, K. Hooman, Thermal assessment of forced convection through metal foam heat exchangers, J. Heat Tran. (2011) 133.

[2] M. Opolot, C. Zhao, M. Liu, S. Mancin, F. Bruno, K. Hooman, Influence of cascaded graphite foams on thermal performance of high temperature phase change material storage systems, Appl. Therm. Eng. (2020) 180.

[3] X. Yang, J. Guo, B. Yang, H. Cheng, P. Wei, Y.-L. He, Design of non-uniformly distributed annular fins for a shell-and-tube thermal energy storage unit, Appl. Energy 279 (2020) 115772.

[4] A. Chumpia, K. Hooman, Performance evaluation of tubular aluminum foam heat exchangers in single row arrays, Appl. Therm. Eng. 83 (2015).

[5] T. Lu, H.A. Stone, M. Ashby, Heat transfer in open-cell metal foams, Acta Mater. 46 (1998) 3619–3635.

[6] C. Zhao, M. Opolot, M. Liu, F. Bruno, S. Mancin, K. Hooman, Numerical study of melting performance enhancement for PCM in an annular enclosure with internal-external fins and metal foams, Int. J. Heat Mass Tran. (2020) 150.

[7] J. Guo, Z. Liu, Z. Du, J. Yu, X. Yang, J. Yan, Effect of fin-metal foam structure on thermal energy storage: an experimental study, Renew. Energy 172 (2021) 57–70.

[8] S.S. Woo, I. Shalev, R.L. Barker, Heat and moisture transfer through nonwoven fabrics: Part I: heat transfer, Textil. Res. J. 64 (1994) 149–162.

[9] D.M. Burke, M.A. Morris, J.D. Holmes, Chemical oxidation of mesoporous carbon foams for lead ion adsorption, Separ. Purif. Technol. 104 (2013) 150–159.

[10] A. Kumar, R. Reddy, Modeling of polymer electrolyte membrane fuel cell with metal foam in the flow-field of the bipolar/end plates, J. Power Sources 114 (2003) 54–62.

[11] W. Li, Z. Qu, Experimental study of effective thermal conductivity of stainless steel fiber felt, Appl. Therm. Eng. 86 (2015) 119–126.

[12] F. Song, Z. Wen, Y. Fang, E. Wang, X. Liu, Combustion wave propagation of a modular porous burner with annular heat recirculation, J. Therm. Sci. 29 (2020) 98–107.

[13] X. Yang, X. Wang, Z. Liu, Z. Guo, L. Jin, C. Yang, Influence of aspect ratios for a tilted cavity on the melting heat transfer of phase change materials embedded in metal foam, Int. Commun. Heat Mass Tran. 122 (2021) 105127.

[14] L. Li, B. Yu, Fractal analysis of the effective thermal conductivity of biological media embedded with randomly distributed vascular trees, Int. J. Heat Mass Tran. 67 (2013) 74–80.

[15] R. McGregor, The effect of rate of flow on rate of dyeing II–The mechanism of fluid flow through textiles and its significance in dyeing, J. Soc. Dye. Colour. 81 (1965) 429–438.

[16] E. Rodriguez, F. Giacomelli, A. Vazquez, Permeability-porosity relationship in RTM for different fiberglass and natural reinforcements, J. Compos. Mater. 38 (2004) 259–268.

[17] A. Costa, Permeability-porosity relationship: a reexamination of the Kozeny-Carman equation based on a fractal pore-space geometry assumption, Geophys. Res. Lett. 33 (2006).

[18] Z. Hashin, S. Shtrikman, A variational approach to the theory of the effective magnetic permeability of multiphase materials, J. Appl. Phys. 33 (1962) 3125–3131.

[19] C.H. Shih, L.J. Lee, Effect of fiber architecture on permeability in liquid composite molding, Polym. Compos. 19 (1998) 626–639.

[20] F. Civan, Scale effect on porosity and permeability: kinetics, model, and correlation, AIChE J. 47 (2001) 271–287.

[21] C. Lawrence, X. Shen, An investigation into the hydraulic properties of needle-punched nonwovens for application in wet-press concrete casting Part II: predictive models for the water permeability of needle-punched nonwoven fabrics, J. Textil. Inst. 91 (2000) 61–77.

[22] D. Shou, J. Fan, F. Ding, Hydraulic permeability of fibrous porous media, Int. J. Heat Mass Tran. 54 (2011) 4009–4018.

[23] Z.G. Qu, T.S. Wang, W.Q. Tao, T.J. Lu, A theoretical octet-truss lattice unit cell model for effective thermal conductivity of consolidated porous materials saturated with fluid, Heat Mass Tran. 48 (2012) 1385–1395.

[24] S. Kuwabara, The forces experienced by randomly distributed parallel circular cylinders or spheres in a viscous flow at small Reynolds numbers, J. Phys. Soc. Jpn. 14 (1959) 527–532.

[25] C. Davies, The separation of airborne dust and particles, Proc. Inst. Mech. Eng. 167 (1953) 185–213.

[26] J.T. Gostick, M.W. Fowler, M.D. Pritzker, M.A. Ioannidis, L.M. Behra, In-plane and through-plane gas permeability of carbon fiber electrode backing layers, J. Power Sources 162 (2006) 228–238.

[27] J. Drummond, M. Tahir, Laminar viscous flow through regular arrays of parallel solid cylinders, Int. J. Multiphas. Flow 10 (1984) 515–540.

[28] B. Yu, L.J. Lee, H. Cao, A fractal in-plane permeability model for fabrics, Polym. Compos. 23 (2002) 201–221.

[29] B. Yu, P. Cheng, Fractal models for the effective thermal conductivity of bidispersed porous media, J. Thermophys. Heat Tran. 16 (2002) 22–29.

[30] C. Zhang, L. Wu, Y. Chen, Study on solidification of phase change material in fractal porous metal foam, Fractals 23 (2015) 1540003.

[31] F. Li, C. Liu, Pressure-transient analysis of two-layers fractal reservoirs, Appl. Math. Mech. 19 (1998) 21–26.

[32] Y. Feng, B. Yu, M. Zou, D. Zhang, A generalized model for the effective thermal conductivity of porous media based on self-similarity, J. Phys. D Appl. Phys. 37 (2007) 3030–3040.

[33] Y.F. Xu, D.A. Sun, A fractal model for soil pores and its application to determination of water permeability, Phys. Stat. Mech. Appl. 316 (2002) 56–64.

[34] T. Zhang, M. Dong, M. Li, A fractal permeability model for shale oil reservoir, IOP Conf. Series: Earth Environ. Sci. IOP Publ. 108 (2018), 032083.

[35] B. Yu, P. Cheng, A fractal permeability model for bi-dispersed porous media, Int. J. Heat Mass Tran. 45 (2002) 2983–2993.

[36] B. Yu, Analysis of flow in fractal porous media, Appl. Mech. Rev. 61 (2008), 050801.

[37] B. Yu, J. Li, A geometry model for tortuosity of flow path in porous media, Chin. Phys. Lett. 21 (2004) 1569.

[38] F. Zhu, S. Cui, B. Gu, Fractal analysis for effective thermal conductivity of random fibrous porous materials, Phys. Lett. 374 (2010) 4411–4414.

[39] S. Sharma, D.A. Siginer, Permeability measurement methods in porous media of fiber reinforced composites, Appl. Mech. Rev. 63 (2010).

[40] B. Yu, J. Li, Some fractal characters of porous media, Fractals 9 (2001) 365–372.

[41] J. Cai, B. Yu, A discussion of the effect of tortuosity on the capillary imbibition in porous media, Transport Porous Media 89 (2011) 251–263.

[42] J. Cai, B. Yu, Prediction of maximum pore size of porous media based on fractal geometry, Fractals 18 (2010) 417–423.

[43] A. Majumdar, B. Bhushan, Fractal model of elastic-plastic contact between rough surfaces, J. Tribol. 113 (1991) 1–11.

[44] A. BY, B. JL, A. ZL, A. MZ, Permeabilities of unsaturated fractal porous media, Int. J. Multiphas. Flow 29 (2003) 1625–1642.

[45] X. Peng, S. Qiu, B. Yu, Z. Jiang, Prediction of relative permeability in unsaturated porous media with a fractal approach, Int. J. Heat Mass Tran. 64 (2013) 829–837.

[46] S. Yang, B. Yu, M. Zou, M. Liang, A fractal analysis of laminar flow resistance in roughened microchannels, Int. J. Heat Mass Tran. 77 (2014) 208–217.

[47] J. Cai, L. Luo, R.A.N. Ye, X. Zeng, X. Hu, Recent advances on fractal modeling of permeability for fibrous porous media, Fractals 23 (2015) 1540006.

[48] A. Koponen, M. Kataja, J. Timonen, Permeability and effective porosity of porous media, Physreve 56 (1997) 3319–3325.

[49] V. Myroshnychenko, C. Brosseau, Finite-element method for calculation of the effective permittivity of random inhomogeneous media, Phys. Rev. E - Stat. Nonlinear Soft Matter Phys. 71 (2005) 16701.

[50] P.A. Fokker, General anisotropic effective medium theory for the effective permeability of heterogeneous reservoirs, Transport Porous Media 44 (2001) 205–218.

[51] H. Okabe, M.J. Blunt, Prediction of permeability for porous media reconstructed using multiple-point statistics, Phys. Rev. 70 (2004) 66135.

[52] B. Yang, W. Wu, M. Li, W. Zhai, A multiple-relaxation-time lattice Boltzmann model for natural convection in a hydrodynamically and thermally anisotropic porous medium under local thermal non-equilibrium conditions, J. Therm. Sci. 29 (2020) 609–622.

[53] B. Yu, M. Zou, Y. Feng, Permeability of fractal porous media by Monte Carlo simulations, Int. J. Heat Mass Tran. 48 (2005) 2787–2794.

[54] A.N. Volkov, L.V. Zhigilei, Thermal conductivity of two-dimensional disordered fibrous materials defined by interfiber thermal contact conductance and intrinsic conductivity of fibers, J. Appl. Phys. 127 (2020) 65102.

[55] A.N. Volkov, L.V. Zhigilei, Scaling laws and mesoscopic modeling of thermal conductivity in carbon nanotube materials, Phys. Rev. Lett. 104 (2010) 215902.

[56] A.N. Volkov, L.V. Zhigilei, Heat conduction in carbon nanotube materials: strong effect of intrinsic thermal conductivity of carbon nanotubes, Appl. Phys. Lett. 101 (2012), 043113.

[57] A. Thompson, A. Katz, C. Krohn, The microgeometry and transport properties of sedimentary rock, Adv. Phys. 36 (1987) 625–694.

[58] Y. Chen, M. Shi, Determination of effective thermal conductivity for real porous media using fractal theory, J. Therm. Sci. 8 (1999) 102–107.

[59] P. Xu, B. Yu, M. Yun, M. Zou, Heat conduction in fractal tree-like branched networks, Int. J. Heat Mass Tran. 49 (2006) 3746–3751.

[60] H. Shen, Q. Ye, G. Meng, Anisotropic fractal model for the effective thermal conductivity of random metal fiber porous media with high porosity, Phys. Lett. 381 (2017) 3193–3196.

[61] P. Adler, Transports in fractal porous media, J. Hydrol. 187 (1996) 195–213.

[62] J. Thovert, F. Wary, P. Adler, Thermal conductivity of random media and regular fractals, J. Appl. Phys. 68 (1990) 3872–3883.

[63] B.B. Mandelbrot, B.B. Mandelbrot, The Fractal Geometry of Nature, WH freeman, New York, 1982.

[64] A. Majumdar, B. Bhushan, Role of fractal geometry in roughness characterization and contact mechanics of surfaces, J. Tribol. (1990).

[65] Y. Pan, G. Xu, W. Li, C. Zhong, A novel numerical cubic filament model and method for the two-energy equation in porous media, Int. J. Heat Mass Tran. 80 (2015) 688–697.

[66] J. Wu, B. Yu, M. Yun, A fractal resistance model for flow through porous media, Int. J. Heat Mass Tran. 71 (2008) 331–343.

[67] B. Yu, Fractal character for tortuous streamtubes in porous media, Chin. Phys. Lett. 22 (2005) 158.

[68] J. Bear, Dynamics of Fluids in Porous Media, Courier Corporation, 2013.

[69] F.A. Dullien, Porous Media: Fluid Transport and Pore Structure, Academic press, 2012.

[70] M. Yun, B. Yu, P. Xu, J. Wu, Geometrical models for tortuosity of streamlines in three-dimensional porous media, Can. J. Chem. Eng. 84 (2006) 301–309.

[71] Y. Ma, B. Yu, D. Zhang, M. Zou, A self-similarity model for effective thermal conductivity of porous media, J. Phys. D Appl. Phys. 36 (2003) 2157.

[72] W.B. Young, K. Rupel, K. Han, L.J. Lee, J.L. Ming, Analysis of resin injection molding in molds with preplaced fiber mats. II: numerical simulation and experiments of mold filling, Polym. Compos. 12 (1991) 30–38.

[73] D.J. Skamser, D.P. Bentz, R.T. Coverdale, M.S. Spotz, N. Martys, H. Jennings, et al., Calculation of the thermal conductivity and gas permeability in a uniaxial bundle of fibers, J. Am. Ceram. Soc. 77 (1994) 2669–2680.

[74] G.W. Jackson, D.F. James, The hydrodynamic resistance of hyaluronic acid and its contribution to tissue permeability, Biorheology 19 (1982) 317–330.

[75] K.H. Stenzel, A.L. Rubin, W. Yamayoshi, T. Miyata, T. Suzuki, T. Sohde, et al., Optimization of collagen dialysis membranes, Am. Soc. Artif. Intern. Organs J. 17 (1971) 293–298.

[76] W.L. Ingmanson, Internal pressure distribution in compressible mats under fluid stress, TAPPI 42 (1959) 840–849.

[77] J. Wheat, The air flow resistance of glass fibre filter paper, Can. J. Chem. Eng. 41 (1963) 67–72.

[78] R. Labrecque, Effects of fiber cross-sectional shape on resistance to flow of fluids through fiber mats, TAPPI (Tech. Assoc. Pulp Pap. Ind.) 51 (1968) 8–15.

[79] M.A. Tahir, H. Vahedi Tafreshi, Influence of fiber orientation on the transverse permeability of fibrous media, Phys. Fluids 21 (2009) 123601.

[80] P.C. Carman, Determination of the specific surface of powders I, Transactions. J Soc Chemical Industries. 57 (1938) 225–234.

[81] J. Brown, Determination of the exposed specific surface of pulp fibers from air permeability measurements, TAPPI (Tech. Assoc. Pulp Pap. Ind.) 33 (1950) 130–137.

[82] M.L. White, The permeability of an acrylamide polymer gel, J. Phys. Chem. 64 (1960) 1563–1565.

[83] R. Viswanadham, D.C. Agrawal, E.J. Kramer, Water transport through reconstituted collagen hollow-fiber membranes, J. Appl. Polym. Sci. 22 (1978) 1655–1663.

[84] J. Happel, Viscous flow relative to arrays of cylinders, AIChE J. 5 (1959) 174–177.

[85] B.R. Gebart, Permeability of unidirectional reinforcements for RTM, J. Compos. Mater. 26 (1992) 1100–1133.

[86] J. Van der Westhuizen, J.P. Du Plessis, An attempt to quantify fibre bed permeability utilizing the phase average Navier-Stokes equation, Compos. Appl. Sci. Manuf. 27 (1996) 263–269.

[87] A. Tamayol, M. Bahrami, Transverse permeability of fibrous porous media, Phys Rev E Stat Nonlin Soft Matter Phys 83 (2011) 46314.

[88] W.J. Mantle, W.S. Chang, Effective thermal conductivity of sintered metal fibers, J. Thermophys. Heat Tran. 5 (1991) 545–549.

[89] N. Haruki, A. Horibe, K. Nakashima, Anisotropic effective thermal conductivity measurement of various kinds of metal fiber materials, Int. J. Thermophys. 34 (2013) 2385–2399.

[90] X. Huang, Q. Zhou, J. Liu, Y. Zhao, W. Zhou, D. Deng, 3D stochastic modeling, simulation and analysis of effective thermal conductivity in fibrous media, Powder Technol. 320 (2017) 397–404.

[91] L. Tadrist, M. Miscevic, O. Rahli, F. Topin, About the use of fibrous materials in compact, heat exchangers 28 (2004) 193–199.

[92] M.G. Semena, V.K. Zaripov, Influence of the diameter and length of fibres on material heat transfer of metal fibre wicks of heat pipes, Therm. Eng. 24 (1977) 69–72.

[93] J. Koh, E. Casal, R.W. Evans, V. Deriugin, Fluid Flow and Heat Transfer in High-Temperature Porous Matrices for Transpiration Cooling, 1966.

[94] C. Veyhl, T. Fiedler, O. Andersen, J. Meinert, T. Bernthaler, I.V. Belova, et al., On the thermal conductivity of sintered metallic fibre structures, Int. J. Heat Mass Tran. 55 (2012) 2440–2448.

[95] H. Shen, Q. Ye, G. Meng, Anisotropic fractal model for the effective thermal conductivity of random metal fiber porous media with high porosity, Phys. Lett. (2017). S0375960117307302.

[96] J.C. Halpin, Stiffness and expansion estimates for oriented short fiber composites, J. Compos. Mater. 3 (1969) 732–734.

[97] A. Acton, Correlating equations for the properties of metal-felt wicks, Adv. Heat Pipe Technol. (1982) 279–288.

[98] E.G. Alexander JR., Structure-property Relationships in Heat Pipe Wicking Materials, North Carolina State University, 1972.

[99] P.J. Berenson, D.W. Graumann, M.M. Soliman, Effective Thermal Conductivity of Dry and Liquid-Saturated Sintered Fiber Metal Wicks, mechanical engineering, 1970.